# Observational Studies on the Turbulent Kinetic Energy Change due to the Nonlinearity of the Fluid Dynamics in the Atmospheric Surface Layer

博士論文

# Observational Studies on the Turbulent Kinetic Energy Change due to the Nonlinearity of the Fluid Dynamics in the Atmospheric Surface Layer

(流体力学の非線形性に由来する乱流運動エネルギー変動の観測的研究)

ISHIDA Sachinobu

石田 祐宣

平成17年

# Contents

# List of Figures

# List of Tables

# Acknowledgments

The author is grateful to Professor N. Yasuda of Tohoku University for his continuous guidance of this research and encouragement. The author wishes to thanks Emeritus Professor J. Kondo of Tohoku University for his guidance to the boundary-layer meteorology, efficient discussion and encouragement. The author would like to thank Professor T. Iwasaki, Dr. W. Sha, Dr. D. Matsushima (also thank for his joining in CAPS), members at Atmospheric Science Laboratory of Tohoku University, Dr. T. Watanabe of the Forestry and Fortest Products Research Institute, Dr. J. Xu of the Frontier Research Center for Global Change, Dr. H. Sugawara of the National Defense Academy of Japan, for their useful comments and discussions, Professor K. Rikiishi and Dr. Y.-M. Kodama of the Hirosaki University for their support and patient encouragement.

Thanks are extended to the FLUX Enthusiasts Party and the CAPS observation members for their dedicated efforts on in the installations and maintenance of the sensors. The author especially thank Dr. K. Tanaka at Kyoto University (administrator of the paddy field site of the Lake Biwa project), Dr. A. Higuchi (Chiba University), Dr. I. Tamagawa (Gifu University), Dr. J. Asanuma (University of Tsukuba), and Dr. T. Hiyama (Nagoya University) for their useful comments and encouragements. Mr. R. Arasawa of Hirosaki University had the courage to join in CAPS. The sensors were kindly provided by the Lower Atmosphere and Precipitation Study (LAPS) and the Rangelands Atmosphere-Hydrosphere-Biosphere Interaction Study Experiment in Northeastern Asia (RAISE) projects of the Core Research for Evolutional Science and Technology (CREST), the Japan Science and Technology Agency (JST) and many other organizations.

# Chapter 1

# Introduction

The atmospheric surface layer is the bottom of the boundary layer where human beings are living, and our lives are related deeply with this layer. On the other hand, from the point of view of the atmosphere, this layer is directly influenced by the presence of the Earth's surface which provides strong forcing, such as friction force and heat. So this layer is the most complicated layer of the troposphere. Turbulence is the symbol of this complexity, and has a important role in this layer: Turbulence generates diffusion, which is related to air pollution and vertical flux such as sensible heat, latent heat, and greenhouse effect gas flux (e.g. $CO_2$, $CH_4$). The sensible and latent heat is energy source of the atmospheric circulation and influences local climates. Therefore, it is necessary to understand the turbulence mechanism in order to describe the physical processes of the air in the surface layer.

Turbulent Kinetic Energy (TKE) is one of the most important statistics of the turbulence. In the surface layer, the TKE of the longitudinal (the prevailing wind direction) component is produced by the vertical shear of the wind and the vertical component is produced by buoyancy, then the TKE is transported and redistributed among the components by fluctuation of the air pressure, finally the TKE is converted into heat by the viscosity and vanished. The TKE equation is derived from the Navier–Stokes (NS) equation. Due to the presence of terms that are derived from the nonlinear terms of the NS equations, the TKE equation cannot be solved analytically. In order to close these equations, the parameterization in each term is required. This is referred to as the turbulent closure problem. Although, many scientists have been attempted to evaluate each term by both the field and numerical experiments, consistent characteristics of the TKE are not completed because of limitation of the accuracy of turbulent sensors and computer capacity. Further, since there are few sensors to measure a fine resolution of air pressure perturbation, the pressure correlation term must be evaluated as a residual term of TKE equation. Thus, many numerical models neglect this term just because of the incompressibility. However, only the transport and redistribution terms which are derived from the nonlinear term can be the important TKE source of the lateral component. In order

to evaluate each term and component of the TKE equation, the intensive observations were performed by using multiple accurate turbulent sensors in this study. Details of this observation is written in Chapter 3.

Since the TKE equation has to be simplified by neglecting the local storage and advection terms in order to reduce the estimation errors, the observed data are filtered with the thresholds related to the constancy and homogeneity. The thresholds are described in Chapter 4.

Since the turbulence is apparently a random motion, a quasi-normal distribution hypothesis was adopted to the equations. If the probability density function of the turbulence is normal (Gaussian), the parameterizations of the turbulence are greatly simplified; all the third-order moments equal 0, and the fourth-order moments can be represented by a summation of second-order moment products. Although the turbulence tends to be isotropic and random in the absence of an external force, the turbulence is not exactly normal because of external forces that produce the turbulence. Examples of these external forces are friction and buoyant forces generated at the Earth's surface. Parameterizations of third- and fourth-order moments with second-order moments are discussed by using field data in Chapter 5.

The TKE equations are usually treated as the summation of each component, and only the vertical component of the pressure correlation term is expressed conventionally. While the total pressure correlation term has been considered as zero, the individual components are not necessarily zero and should redistribute the TKE isotropically beyond the components because each component of the TKE budget is closed. In Chapter 6, each component and term of TKE equations for the lowest surface boundary layer is evaluated using the screened data in Chapter 4. The pressure correlation terms are evaluated as the residual of the other terms measured accurately. The characteristics and functions of the pressure correlation terms are discussed.

The sensible heat flux under natural convective conditions, in which TKE is dominantly produced by the buoyancy rather than the wind shear, is one of the most important parameter to understand the mechanism of the convection. However, there have been only a few studies concerning the sensible heat flux under these conditions, due to the difficulty in observing the necessary meteorological elements. In Chapter 7, an attempt is made to parameterize the sensible heat flux under natural convective conditions by analyzing indoor experiments and field observations. Further, the most optimal ratio of horizontal and vertical length of surface roughness elements for efficient sensible heat flux is also discussed together with the results of Chapter 6.

# Chapter 2

# Second-order Equations of Turbulence

## 2.1 Introduction

Since turbulence is a flow regime characterized by semi-random property, each turbulent motion can't be described by deterministic equations. So the turbulent motion is expressed by stochastic parameters. Turbulent Kinetic Energy (TKE) is one of the most important statistics of the turbulence. In order to keep equilibrium conditions of turbulence in viscous fluid, TKE budget, consists of production, transport, and dissipation terms, must be balanced.

In 1968, extensive boundary layer field experiments were performed. The experiment site was flat area in southwest Kansas. Wyngaard et al. (1971) evaluates each term of TKE equation using these data. The energy budget simplifies under horizontally homogeneous conditions, where mean quantities depend only on the vertical coordinate $x_3$, and the mean velocity has only the prevailing wind direction component $\overline{U_1}$. The steady-state TKE budget is expressed as:

$$-\overline{u_1' u_3'}\frac{\partial \overline{U_1}}{\partial x_3} + \frac{g}{\Theta_v}\overline{u_3'\theta_v'} - \frac{1}{2}\frac{\partial \overline{u_3' q^2}}{\partial x_3} - \frac{1}{\rho_0}\overline{u_3'\frac{\partial p'}{\partial x_3}} - \varepsilon = 0, \tag{2.1}$$

details of the parameters are displayed in next section.

In order to evaluate each term and component of the TKE equation in 3 dimension, first of all, TKE equations are derived in each component.

## 2.2 Second-order Moments of Turbulent Fluctuations

By assuming incompressible fluid ($\partial u_k/\partial x_k = 0$), Boussinesq's approximation, and neglecting Coriolis force, the equation of motion (Navier-Stokes (NS) equation) in Einstein's summation notation is written as:

$$\frac{\partial u_i}{\partial t} + u_k\frac{\partial u_i}{\partial x_k} + \frac{1}{\rho_0}\frac{\partial p}{\partial x_i} - \nu\frac{\partial^2 u_i}{\partial x_k^2} - \frac{g}{\Theta_v}\delta_{i3}\theta_v = 0, \tag{2.2}$$

where $\rho_0$ is the reference air density, $\nu$ is the kinematic molecular viscosity, $\delta$ is Kronecker's delta, $g$ is the gravitational acceleration, and $\Theta_v$ is the virtual potential temperature of the environment. The three components of the wind speed $u_i$, virtual potential temperature $\theta_v$ and air pressure $p$ are divided into mean and turbulent parts:

$$\begin{aligned} u_i &= \overline{U_i} + u_i' \qquad (i = 1, 2, 3), \\ \theta_v &= \overline{\theta_v} + \theta_v', \\ p &= \overline{p} + p'. \end{aligned} \tag{2.3}$$

The axis of $i = 1$ is in the longitudinal (the prevailing wind) direction, and those of $i = 2, 3$ are in the lateral and vertical directions, respectively. Then the turbulent part of equation (2.2) is written as:

$$\frac{\partial u_i'}{\partial t} + \overline{u_k}\frac{\partial u_i'}{\partial x_k} + u_k'\frac{\partial \overline{u_i}}{\partial x_k} - \overline{u_k'\frac{\partial u_i'}{\partial x_k}} + u_k'\frac{\partial u_i'}{\partial x_k} + \frac{1}{\rho_0}\frac{\partial p'}{\partial x_i} - \nu\frac{\partial^2 u_i'}{\partial x_k^2} - \frac{g}{\Theta_v}\delta_{i3}\theta_v' = 0. \tag{2.4}$$

The equations for the second-order moment of the turbulent part of the wind speed $R_{ij}$ can be expressed as follows:

$$\begin{aligned} &\frac{\partial R_{ij}}{\partial t} + \overline{U_k}\frac{\partial R_{ij}}{\partial x_k} + \left(R_{ik}\frac{\partial \overline{U_j}}{\partial x_k} + R_{jk}\frac{\partial \overline{U_i}}{\partial x_k}\right) - \frac{g}{\Theta_v}\left(\delta_{j3}R_{i\theta} + \delta_{i3}R_{j\theta}\right) \\ &\quad + \frac{\partial R_{ijk}}{\partial x_k} + \frac{1}{\rho_0}\left(\overline{u_i'\frac{\partial p'}{\partial x_j}} + \overline{u_j'\frac{\partial p'}{\partial x_i}}\right) - \nu\left(\overline{u_j'\frac{\partial^2 u_i'}{\partial x_k^2}} + \overline{u_i'\frac{\partial^2 u_j'}{\partial x_k^2}}\right) = 0, \end{aligned} \tag{2.5}$$

where $R_{ij}, R_{i\theta}$ and $R_{ijk}$ represent $\overline{u_i'u_j'}, \overline{u_i'\theta_v'}$ and $\overline{u_i'u_j'u_k'}$, respectively. The first term of equation (2.5) is local storage of covariance, the second is the advection of covariance, the third is a shear production term, the fourth is a buoyant production term, the fifth is a turbulent transport term ($R_{ij}$ is transported by the turbulent eddies $u_k'$), the sixth is a pressure correlation term redistribute covariance by pressure perturbations, and the final is a viscous dissipation term.

Equation (2.5) contains an unknown higher-order turbulent transport term. In order to close these equations, the parameterization in each term is required. In the case of $i = j$, equation (2.5) yields three components of the TKE equations or the variance of the wind speed as follows:

$$\frac{\partial R_{ii}}{\partial t} + \overline{U_j}\frac{\partial R_{ii}}{\partial x_j} + 2R_{ij}\frac{\partial \overline{U_i}}{\partial x_j} - \frac{2g}{\Theta_v}\delta_{i3}R_{i\theta} + \frac{\partial R_{iij}}{\partial x_j} + \frac{2}{\rho_0}\overline{u_i'\frac{\partial p'}{\partial x_i}} - 2\nu\overline{u_i'\frac{\partial^2 u_i'}{\partial x_j^2}} = 0. \tag{2.6}$$

## 2.3 Turbulent Kinetic Energy (TKE) Equations

Under stationary and horizontally homogeneous conditions, with the exception of the pressure correlation term, each component of (2.6) is written as

$$\begin{aligned} -\overline{u_1'u_3'}\frac{\partial \overline{U_1}}{\partial x_3} &- \frac{1}{2}\frac{\partial \overline{u_1'^2 u_3'}}{\partial x_3} - \frac{1}{\rho_0}\overline{u_1'\frac{\partial p'}{\partial x_1}} - \frac{1}{3}\varepsilon = 0, \\ &- \frac{1}{2}\frac{\partial \overline{u_2'^2 u_3'}}{\partial x_3} - \frac{1}{\rho_0}\overline{u_2'\frac{\partial p'}{\partial x_2}} - \frac{1}{3}\varepsilon = 0, \\ \frac{g}{\Theta_v}\overline{u_3'\theta_v'} &- \frac{1}{2}\frac{\partial \overline{u_3'^3}}{\partial x_3} - \frac{1}{\rho_0}\overline{u_3'\frac{\partial p'}{\partial x_3}} - \frac{1}{3}\varepsilon = 0, \end{aligned} \tag{2.7}$$

where $\varepsilon \left(= \nu\overline{u_i'(\partial^2 u_i'/\partial x_j^2)}\right)$ is the dissipation rate. The first shear production term remains only in the $x_1$-component because of the assumption of the horizontal homogeneity. And the buoyant production term is only in the $x_3$-component. Since there are no production term in the $x_2$-component and the dissipation term is always negative, the turbulent transport and pressure correlation terms can be TKE source.

The shear production term can be expressed in terms of the non-dimensional wind shear function of the Monin–Obukhov similarity theory:

$$\phi_{\mathrm{M}}(\zeta) = \frac{kx_3}{u_*}\frac{\partial \overline{U_1}}{\partial x_3}, \tag{2.8}$$

where $u_* = \left|-\overline{u_1'u_3'}\right|^{1/2}$ is the friction velocity, $k$ is the von Kármán constant, $\zeta = x_3/L$, and $L = -u_*^3\Theta_v/\left(kg\overline{u_3'\theta_v'}\right)$ is the Obukhov length. Thus, each component of (2.7) multiplied by $kx_3/u_*^3$ should be a function of $\zeta$:

$$\begin{aligned} \phi_{\mathrm{M}}(\zeta) &- \frac{kx_3}{2u_*^3}\frac{\partial \overline{u_1'^2 u_3'}}{\partial x_3} - \frac{kx_3}{\rho_0 u_*^3}\overline{u_1'\frac{\partial p'}{\partial x_1}} - \frac{1}{3}\phi_\varepsilon = 0, \\ &- \frac{kx_3}{2u_*^3}\frac{\partial \overline{u_2'^2 u_3'}}{\partial x_3} - \frac{kx_3}{\rho_0 u_*^3}\overline{u_2'\frac{\partial p'}{\partial x_2}} - \frac{1}{3}\phi_\varepsilon = 0, \\ -\zeta &- \frac{kx_3}{2u_*^3}\frac{\partial \overline{u_3'^3}}{\partial x_3} - \frac{kx_3}{\rho_0 u_*^3}\overline{u_3'\frac{\partial p'}{\partial x_3}} - \frac{1}{3}\phi_\varepsilon = 0, \end{aligned} \tag{2.9}$$

where $\phi_\varepsilon = kx_3\varepsilon/u_*^3$ is the normalized dissipation rate. Each term and component of the TKE equations are estimated as a function of $\zeta$ in this study.

## 2.4 Parameterizations of the Nonlinear Derivative Term

Although the TKE equation is a second-order moment equation, the turbulent transport and pressure correlation terms are third-order moments. (This is the dimension of

$p'/\rho_0$ is equal to that of $u'^2$.) These terms are derived from the nonlinear terms –the advection and pressure terms– of equation (2.2). Hence, the number of unknowns in the set of TKE equations is greater than the number of equations, and the set of equations is not closed. In order to close this equation, the higher-order moments must be parameterized by the lower-order moments.

Mellor and Yamada (1974) describe one of the closure models: the turbulence in the atmospheric surface boundary layers. The level 4 model of Mellor and Yamada (1974) calculates all the terms in the second-order turbulent equations (i.e., equation (2.5)). In this model, the turbulent transport and pressure correlation terms are parameterized by the second-order moments. The parameterizations are based on Mellor (1973) and Rotta (1951).

The turbulent transport term is described as

$$\overline{u_k' u_i' u_j'} = -q\lambda_1 \left( \frac{\partial \overline{u_i' u_j'}}{\partial x_k} + \frac{\partial \overline{u_i' u_k'}}{\partial x_j} + \frac{\partial \overline{u_j' u_k'}}{\partial x_i} \right), \tag{2.10}$$

where $q \equiv \left(\overline{u_i'^2}\right)^{1/2}$ and $\lambda_1$ is an empirical length parameter. For the case of TKE ($i = j, k = 3$) and assuming horizontal homogeneity, this term can be written as

$$\overline{u_i'^2 u_3'} = -q\lambda_1 \left( \frac{\partial \overline{u_i'^2}}{\partial x_3} + 2\delta_{i3} \frac{\partial \overline{u_i'^2}}{\partial x_i} \right). \tag{2.11}$$

This implies that each component of the turbulent transport term is proportional to the second-order derivative of TKE with respect to height.

The pressure correlation term is described as

$$-\frac{1}{\rho_0} \left( \overline{u_i' \frac{\partial p'}{\partial x_j}} + \overline{u_j' \frac{\partial p'}{\partial x_i}} \right) = -\frac{q}{3l_1} \left( \overline{u_i' u_j'} - \frac{\delta_{ij}}{3} q^2 \right) + Cq^2 \left( \frac{\partial \overline{U_i}}{\partial x_j} + \frac{\partial \overline{U_j}}{\partial x_i} \right), \tag{2.12}$$

where $l_1$ and $C$ are empirical constants. For the case of $i = j$, as in the case of the turbulent transport term, the pressure correlation term can be written as

$$-\frac{1}{\rho_0} \left( \overline{u_i' \frac{\partial p'}{\partial x_j}} + \overline{u_j' \frac{\partial p'}{\partial x_i}} \right) = -\frac{q}{3l_1} \left( \overline{u_i'^2} - \frac{q^2}{3} \right). \tag{2.13}$$

The summation of all the components of equation (2.13) is equal to zero. Therefore, larger TKE component redistribute the energy to smaller components.

These terms are assumed to be smaller and are parameterized in accordance with the old hypothesis. However, these parameterizations have not been confirmed with accurate sensors that were recently developed. If the turbulent model is required to be used for finer resolutions such as that of a street canyon or around tree leaves, these terms cannot be neglected. This concept is the basic premise of the current study.

## 2.5 Concluding Remarks

The second-order and TKE equations in each component are derived from the NS equations. Due to the presence of terms that are derived from the nonlinear term of the NS equations, TKE equations cannot be solved analytically. Parameterizations of these terms were attempted by Mellor and Yamada (1974) based on the hypothesis of Rotta (1951) and Mellor (1973). However, there in no experimental proof yet.

According to equations (2.9), TKE of the $x_2$-component must be redistributed through the turbulent transport and/or pressure correlation terms. Therefore, these terms must be evaluated in order to understand the TKE properties of the $x_2$-component. In Chapter 6, each term of equations (2.9) is evaluated by using field data.

# Chapter 3

# Field Experiments

## 3.1 Introduction

In order to understand the land-atmosphere interaction, and the energy and water cycles, many observational projects have been held and are in progress. Meanwhile there have been many problems related to the Atmospheric Boundary Layer (ABL) observation as follows:

**The energy (heat) imbalance:** the underestimation of the turbulent heat (the sensible and latent heat $H + lE$) flux compared to the forcing heat (the net radiation $Rn$ minus the conductive soil heat flux $G$).

**Footprint:** the source area or the distribution of it's contribution ratio of turbulent flux.

**Stationary convection (plume):** although over the homogeneous surface, buoyant flow tends to occur in the same area.

**Averaging time:** if there is long period turbulence, too short averaging time to estimate turbulent flux would provoke underestimation.

The energy imbalance could be caused by the latter three problems.

The *Flux Enthusiasts Party* consists of those who are interested in such problems and the turbulence in ABL. The intensive integrated ABL observation has been carried out by together with the *Flux Enthusiasts Party* and the *Lake Biwa Project* at the paddy field site of the *Lake Biwa Project.* The *Lake Biwa Project* has been developed and proceeded by a Japanese group for investigating the hydrological cycle near land surface. This observation was called CAPS (Catch A Plume by SATs; SAT is the Sonic Anemometer-Thermometer) because over 16 SATs were used in order to understand the dynamic structure of the plume and the convection in the surface layer.

The observation has been carried out twice, in 2002 (CAPS2002) and 2003 (CAPS2003) autumn. In CAPS2002 and 2003, the distance of each SAT was $O$ (100m) and $O$ (10m) respectively. The surface source area for the heat flux of each site in CAPS2002 were independent whereas the ones in CAPS2003 could be overlapped. Thus, the dynamic structure throughout scale from 10m to 1km will be resolved by using the data. In this chapter, the distribution of the sensible heat flux and the heat balance is analyzed, and confirmed the horizontal homogeneity. (This chapter is partly cited from Ishida et al. (2004a) and Ishida et al. (2004b).)

## 3.2 Inter-comparison of the Turbulent Sensors

Before intensive observation using various types of SATs, the difference among the outputs of these sensors must be evaluated because of flow distortion problem: difference of the shape of SAT probes may affect the outputs (Kaimal et al., 1990; Wieser et al., 2001). Inter-comparison field experiment was carried out at Terrestrial Environment Research Center (TERC), University of Tsukuba, from the middle of May to the beginning of June, 2001. This period was characterized by growing season of grass and high latent heat exchange. Footprint analysis was performed to evaluate the correspondence between the spatial variation of surface skin temperature and the sensible heat fluxes obtained at the measurement site. The surface skin temperature obtained by an infrared imaging camera together with sensible heat fluxes measured at two points, 3m apart from each other, were used in the analysis. A significant correlation was not found between the surface skin temperatures and the sensible heat fluxes, thus the surface in the upwind direction was assumed to be homogeneous. Comparison was made using standard deviations and covariances of the turbulent variables.

A good agreement was found among all the sonic anemometer-thermometers (DA-600, Kaijo; 1210R3, Gill; ATI-SATI). The difference of statistics of these outputs is shown in Table 3.5. And the fast response hygrometer/$CO_2$ analyzers (LI-7500, Li-Cor; OP2, Data Design Group) got data stably. The errors of LI-7500 and OP2 sensors were reduced by simple recalibration using non-fast response hygrometer (Humicap). Underestimation of flux was occurred only when the correlation coefficient of two sensors' output for the band of dynamic calibration was small (Ishida et al., 2004a).

## 3.3 CAPS (Catch A Plume by SATs)

The intensive observations were performed during November 9 to 22, 2002 and October 1 to 10, 2003. Both periods were after harvest because the homogeneous surface and the greater sensible heat flux conditions were expected during these periods. The site was located near Lake Biwa in northern Shiga prefecture, JAPAN (Figure 3.1). Prevailing wind direction was parallel to the paths between paddy fields, southerly (lake breeze) in daytime and northerly (land breeze) in nighttime under clear sky conditions. Figure 3.1 shows the distribution of turbulent sensors. These distribution were oriented parallel to the prevailing wind directions.

The SATs used in CAPS were composed of 10 sets of DA-600 (Kaijo), more than 2 sets of 1210R3 (Gill) and a set of SAT-550 (Kaijo) and other types. Particularly, the outputs of DA-600 and 1210R3 were confirmed that their outputs were almost the same in section 3.2. Installed sensors are listed in Appendix A.2. Characteristics of each year are described as follows.

### 3.3.1 CAPS2002

In CAPS2002, there were 15 SAT sites using 17 SATs in order to measure the heterogeneity of the heat flux. At every site, the installation height of SATs were about 2.5m. 4 of them (C1, C2, C4, C5 site) were with the open-path infrared gas analyzers, and SATs were installed at 3 heights (1.00, 2.45, 5.90m) only at C4 site (see also Table A.2). To complete the rest term of the heat balance, other sensors were installed at C sites, only the sensors of C4 site worked well. The measurement area was extended 500×1500m horizontally. Also surface temperature images were taken by the infrared camera from airplane in November 17, 19, 20 under clear sky conditions. And the upper ABL sounding was held using a sonde and two SODARs. Further details of observation were described in Tamagawa et al. (2004).

During the observational period, typical pressure pattern of Japanese winter was dominated, so the northerly wind was prevailing. In clear conditions, however, the wind direction is followed by the local circulation: the southerly wind blew from the Lake Biwa in daytime. Other meteorological conditions are shown in Figure 3.2.

### 3.3.2 CAPS2003

In CAPS2003, there were 11 SAT sites using 16 SATs to make SAT array. Common SAT installation height was 2.5m the same as CAPS2002. C, S1, N1, E1, W1 sites were with the open-path infrared gas analyzers, and SATs were installed at 3 heights (1.25,

2.50, 5.00m) at C, S3, N3 sites (see also Table A.2). The most different point from CAPS2002 was that the measurement area was concentrated about 100×200m, centered at C2 site (called intensive paddy field) of CAPS2002. Since each tract of paddy field is about 30m width and 100m length, multiple SATs were in the same tract. Photo 3.1 shows the installed SATs. Fine wire thermocouples were used to detect the passing plume near the surface. Surface temperature distribution was measured manually by the two infrared thermometer. The upper ABL sounding was held using a sonde, two SODARs and a doppler lidar.

The meteorological conditions of CAPS2003 are shown in Figure 3.3. The air temperature was higher than CAPS2002. During first two days, the northerly wind was dominated. After that, relatively calm conditions were continued.

## 3.4 Heat Balance and Distribution of the Sensible Heat Flux

Each term of the heat balance equation:

$$Rn - G = H + lE \tag{3.1}$$

was measured independently and averaged for each hour. The net radiation $Rn$ was measured by the pyranometers and the infrared radiometers. Since both observations were performed in less than 2km horizontal scale, downward radiation was assumed to be homogeneous in the area. Upward radiation, however, depended on the surface conditions such as the albedo and the surface temperature. The soil heat flux $G$ was measured by the heat plates. And the sensible and the latent heat flux $H, lE$ was measured by the SATs and the infrared gas analyzers (e.g. LI-7500, Li-Cor). After the simple calibration of the absolute humidity $a$ (Ishida et al., 2004a), and the double axis rotations ($\overline{u_3} = 0$; see Section 4.2), the eddy correlation method ($H = c_p \rho \overline{u_3' \theta'}$, $lE = l\overline{u_3' a'}$) was applied. to estimate the turbulent heat flux. In this study, the heat balance closure ratio is defined as the ratio of the left term to the right term of the heat balance equation (3.1).

### 3.4.1 CAPS2002

Only at C4 site, all terms of the heat balance equation (3.1) were measured successfully. But the imbalance heat flux was up to 100Wm$^{-2}$ around the noon (Figure 3.4), and the closure ratio was 60%. The heat imbalance of CAPS2002 might depend on the distribution of the surface conditions. The surface of C4 site was dark and wet. The albedo of this

site was 5∼10% lower than the other sites, that means the net shortwave radiation input was nearly 55Wm$^{-2}$ lower around C4 site because the maximum incoming insolation was 550Wm$^{-2}$. And the maximum difference of the surface temperature was about 2 ℃ in the observation region (Figure 3.5). It might affect $G$, $H$ smaller and $lE$ larger. All of these factors could make the local heat imbalance, but they don't explain all of the maximum imbalance (100Wm$^{-2}$) explicitly.

Figure 3.6 shows the distribution map of the sensible heat flux and the surface temperature. The surface temperature was measured by the infrared camera (Inframatics, MODEL740) mounted on the airplane, and made calibration and correction of the geometry, the viewing angle and the medium atmosphere, then combined by the multiple shot. The difference of the sensible heat flux between each site was almost equal to the random error, and was about 30% of mean flux (77W/m$^2$) during 9-15 local time under clear conditions (Matsushima et al., 2004). The difference seems to be correspond to the surface temperature distribution.

Flux footprint analysis of Kormann and Meixner (2001) were applied to CAPS2002. $T_s$ of the source area was calculated by the surface temperature in the footprint area. The footprint areas were spread northward, because northerly wind was blowing at that time. However each shapes were different by the influence of the local wind distribution. According to the relationship between $U(T_S - T)$ and the sensible heat flux $H$, the sensible heat flux was correlated with the product of the temperature difference between the surface and the air $T_S - T$ and the wind speed $U$. The slope of the data means the bulk coefficient for heat $C_H$ (see equation (7.1)), which was almost unity through unstable conditions. These results suggest that local sensible heat flux was determined by the bulk relation of $U(T_S - T)$ in the footprint area of each site (Matsushima et al., 2004).

### 3.4.2 CAPS2003

In order to measure greater spatial difference of the sensible heat, CAPS2003 was carried out 1 month earlier than CAPS2002. So the maximum net insolation was 50Wm$^{-2}$ larger, and the surface temperature was 10 ℃ higher than CAPS2002. Since the observation region was smaller, the difference of the upward shortwave and longwave radiation was smaller. The maximum difference of the soil heat flux $G$ was 50Wm$^{-2}$. Thus the surface conditions must have been more homogeneous than CAPS2002. The difference ratio of the sensible heat flux was a little smaller than CAPS2002 (Figure 3.7), and was almost equal to the random error.

The heat balance was roughly closed in CAPS2002; the average closure ratio was 100%

whereas the deviation was up to $100\mathrm{Wm}^{-2}$ (Figure 3.8). These results suggests that the heat balance would be closed using the data measured at multiple points under thermally homogeneous surface conditions.

## 3.5 Concluding Remarks

In order to obtain the turbulent data confirmed the horizontal homogeneity, the intensive observations using multiple SATs were performed on the uniform paddy field in 2002 and 2003. It is found that even on apparently homogeneous surface, the sensible heat flux is different among the sites. Therefore, the heat imbalance is likely occurred by the one point observation. Followings are possible reasons:

- There are slight heterogeneity of the thermal surface conditions; albedo, the surface wetness and temperature, even on *apparently* homogeneous surface.
- The spatial difference of the turbulent heat flux is determined by the local difference of the surface temperature and wind speed caused by the plume in a few hundred meter scale.

In CAPS2002, the difference of the sensible heat flux $H$ is correlated with $U(T_\mathrm{S} - T)$, and the each term of measured heat was not closed. Thus, the homogeneity of the turbulence is not verified in CAPS2002. On the contrary, the heat balance was closed in CAPS2003. Therefore, the data of CAPS2003 is used for evaluation of each term of TKE.

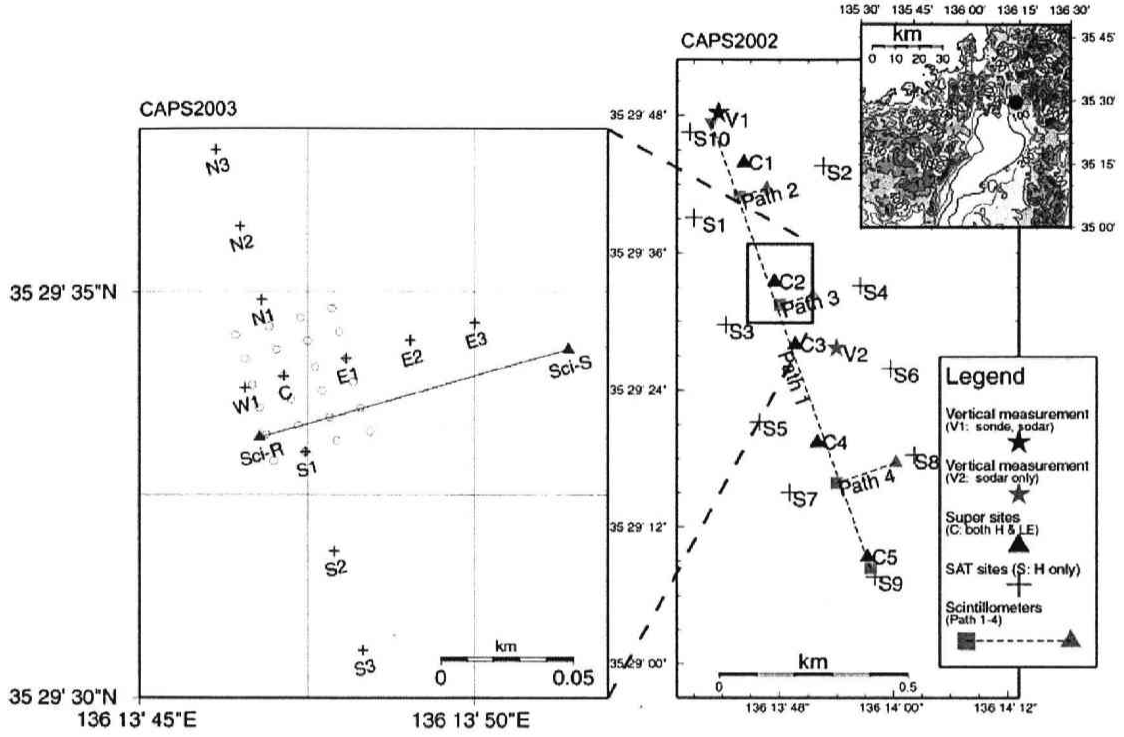


Figure 3.1: Turbulent sensors' distribution map of CAPS2002, 2003. (Right panel) CAPS2002: Legend is indicated in map. (Left panel) CAPS2003: +: SAT site (C, S3, N3: 3 heights; C, S1, N1, E1, W1: with water vapor sensor), ○: fine wire thermocouple site. The line between ▲ shows scintillometer path.

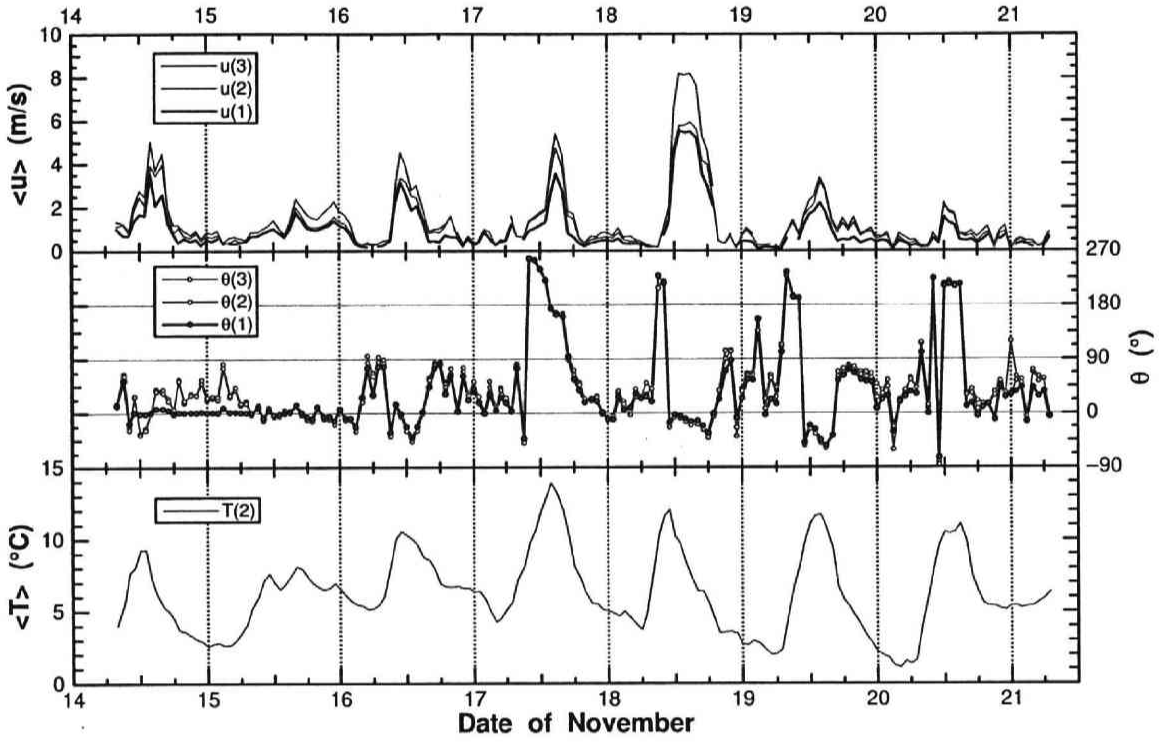


Figure 3.2: Meteorological conditions at C4 site of CAPS2002. (Top panel) wind speed, (Middle panel) wind direction, (Bottom panel) air temperature.

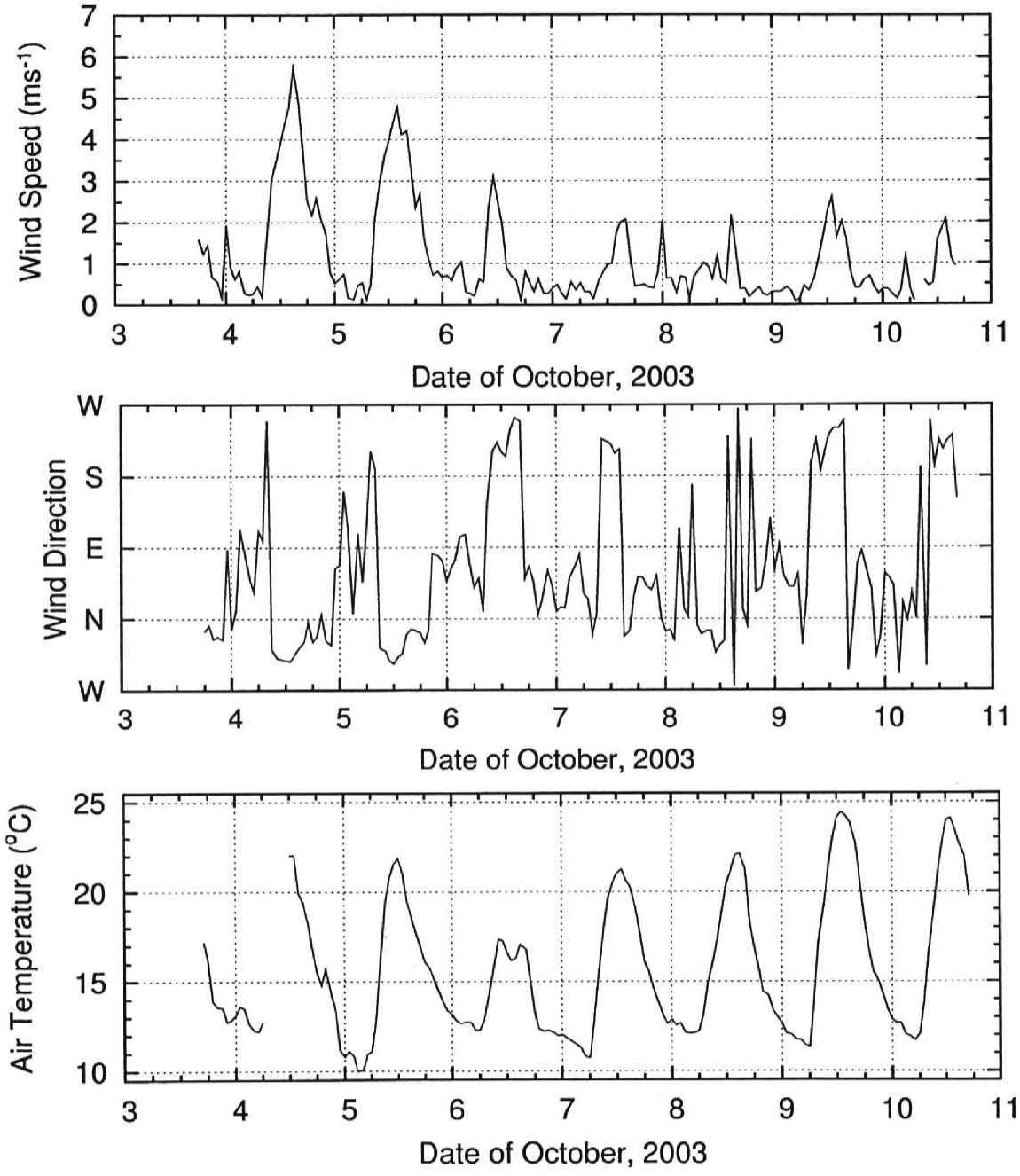


Figure 3.3: Meteorological conditions at C site of CAPS2003. (Top panel) wind speed, (Middle panel) wind direction, (Bottom panel) air temperature.

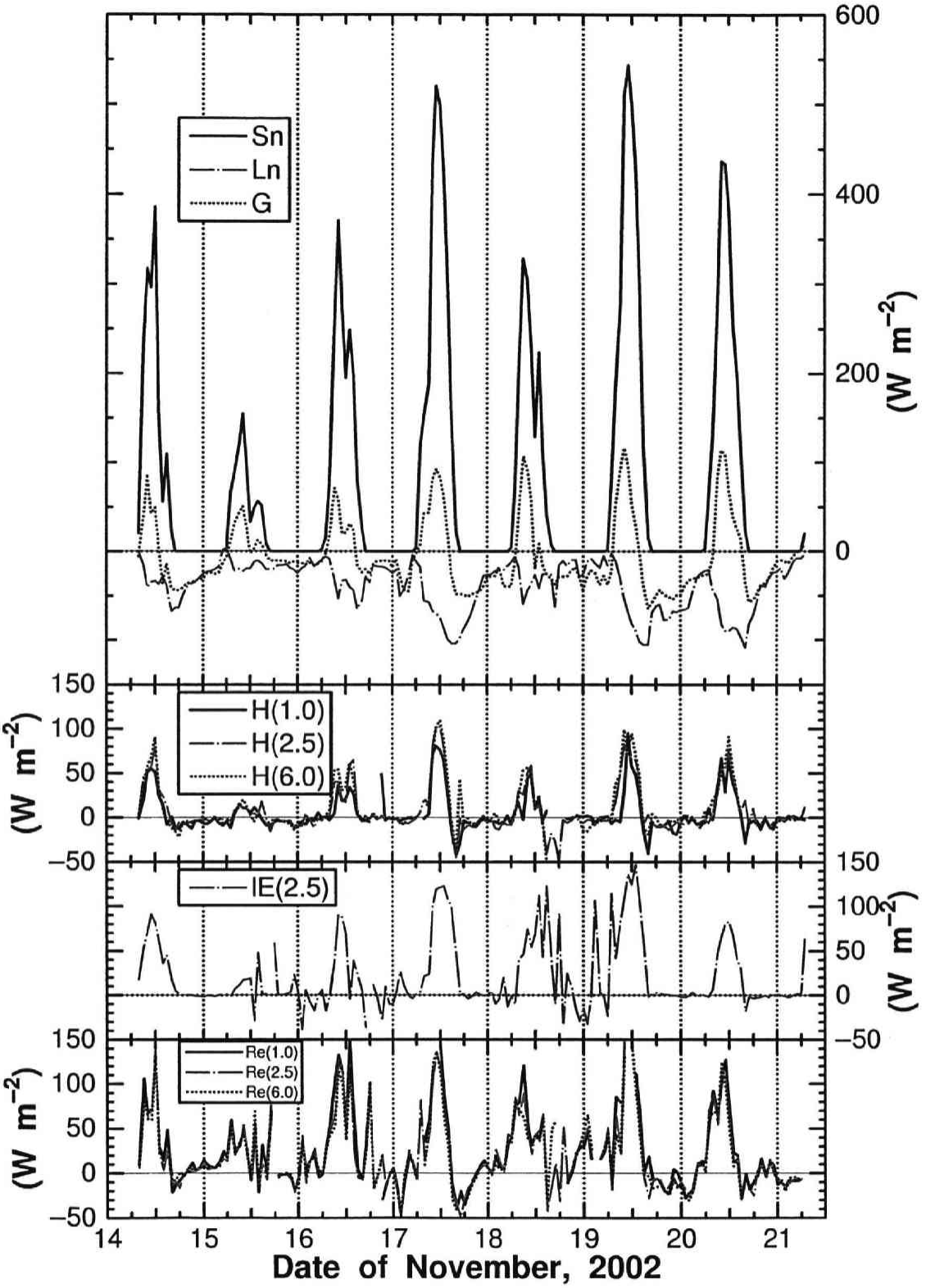


Figure 3.4: Each term of the heat balance and the residual term of CAPS2002 at C4 site (3 heights; 1.0, 2.5, 6.0m). *Sn*: net insolation, *Ln*: net longwave radiation, *G*: soil heat flux, *H*: sensible heat flux, *lE*: latent heat flux, *Re*: residual term of right member of equation (3.1).

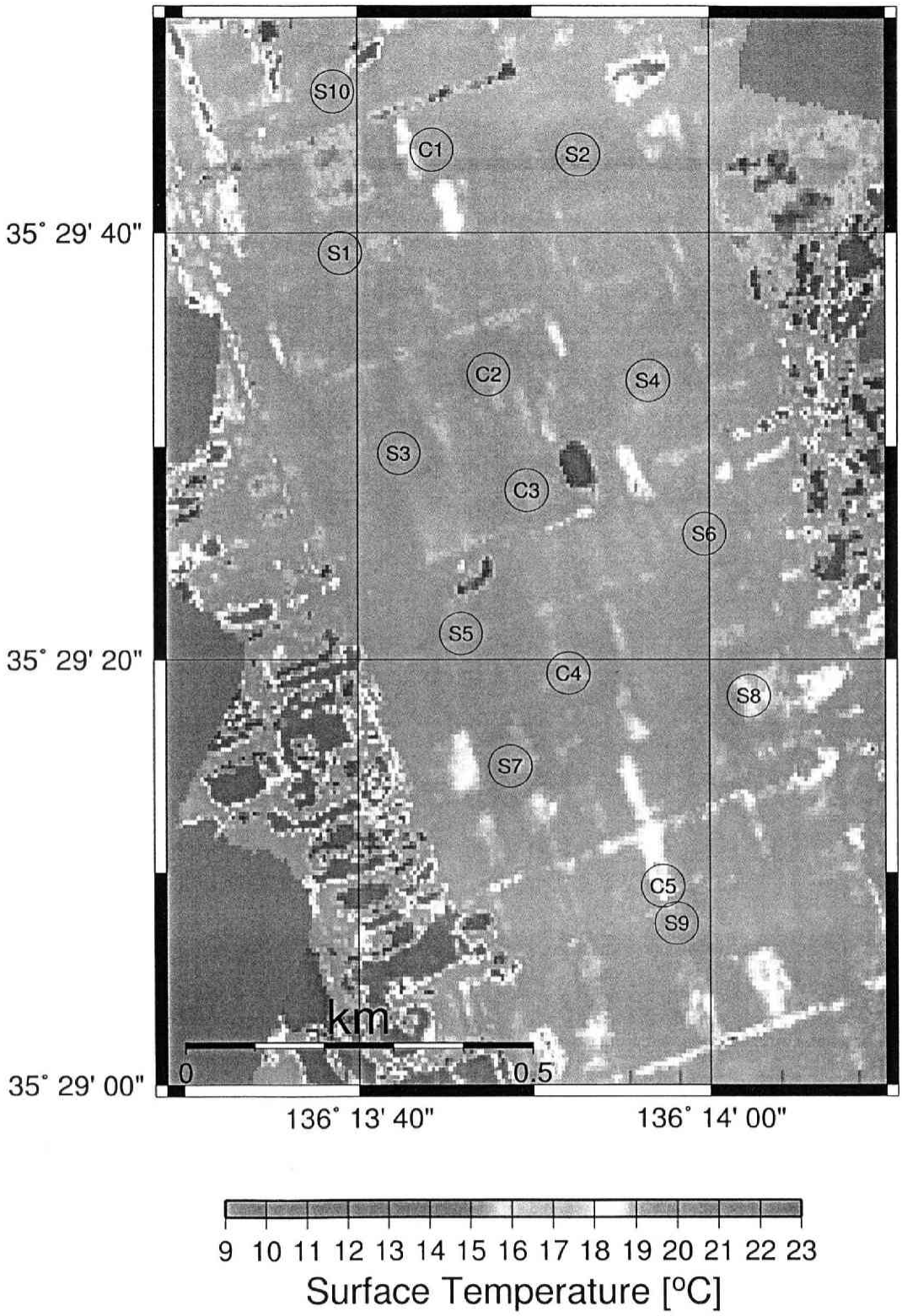


Figure 3.5: Distribution map of the surface temperature for 11:35 to 11:58JST, Nov. 17, 2002. After Tamagawa et al. (2004).

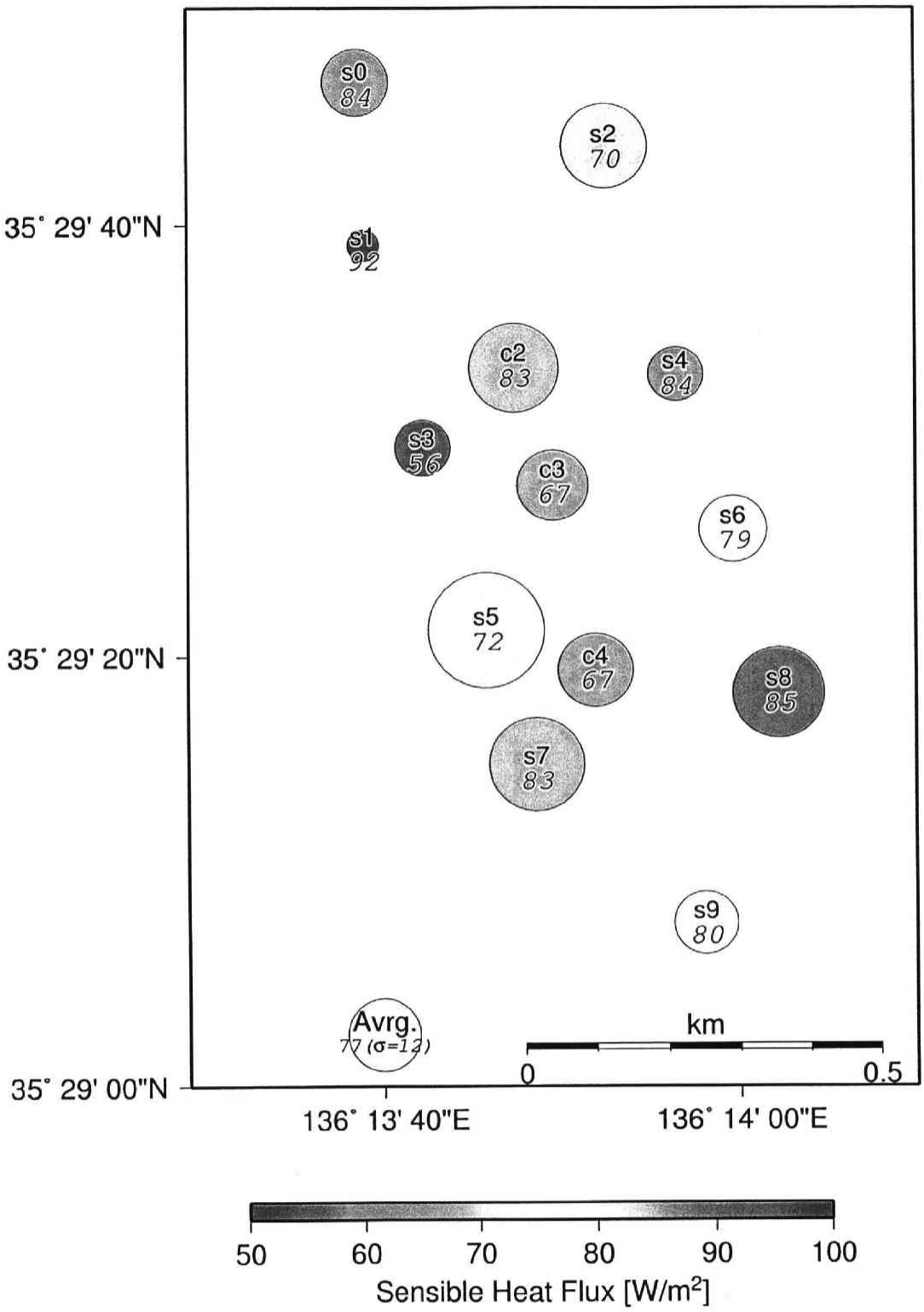


Figure 3.6: Distribution map of the daytime average sensible heat flux for 9 to 15JST, Nov. 17, 19, 20, 2002.

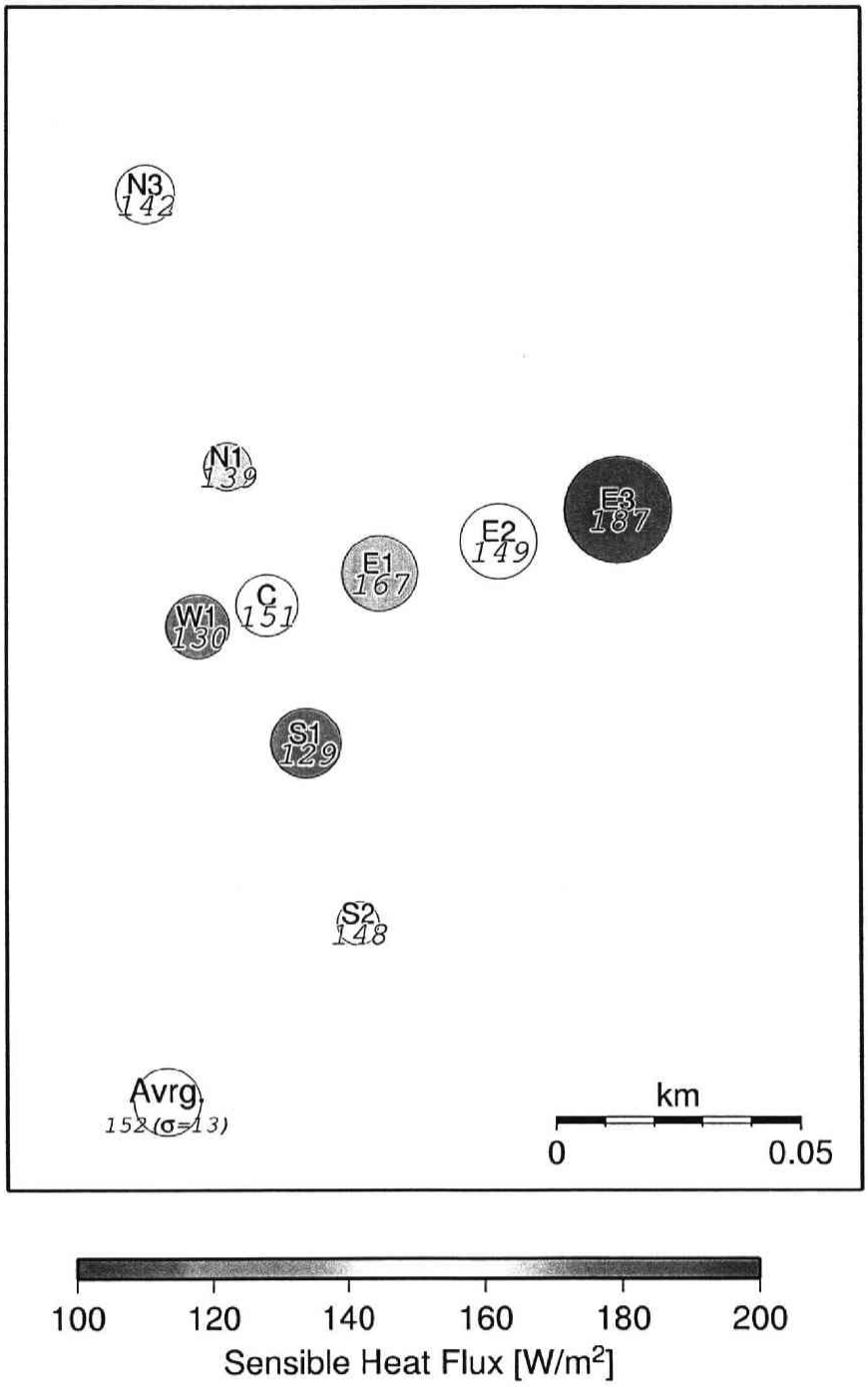


Figure 3.7: Distribution map of the daytime average sensible heat flux for 9 to 15JST, Oct. 5, 7, 9, CAPS2003.

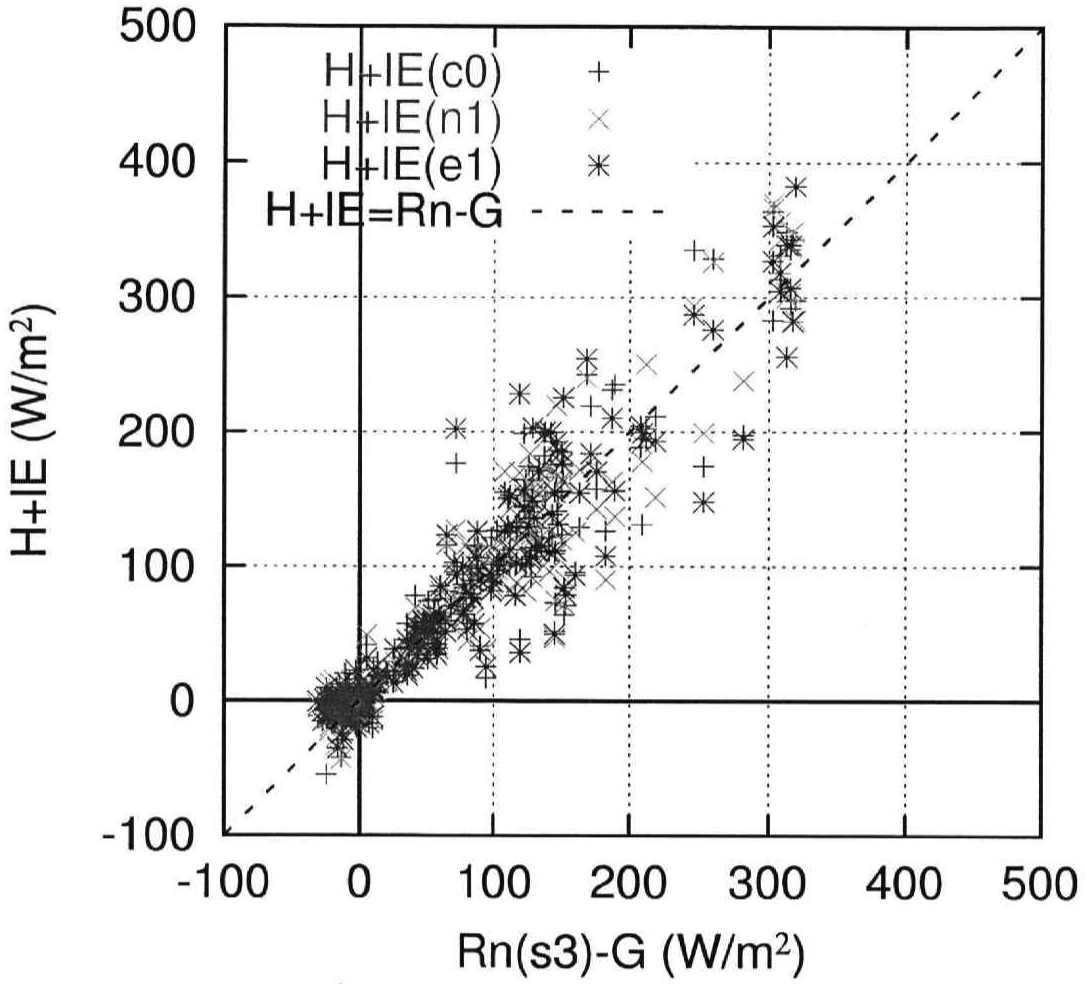


Figure 3.8: Heat balance of C, N1, E1 site in CAPS2003. The data of net radiation at S3 site was referred.

Table 3.1: Inter-comparison of turbulence statistics of sonic anemometer-thermometers. (d) means the data were limited by wind direction. S.D.: standard deviation, n: number of the data. After Ishida et al. (2004).

| | **DA-600-3T** | **GILL** | | | **DA-600-1T** | | | **ATI** | | |
|---|---|---|---|---|---|---|---|---|---|---|
| | | slope | (S.D.) | [n] | slope | (S.D.) | [n] | slope | (S.D.) | [n] |
| $\sigma_w$ | 1 | 0.90 | (0.014) | [300] | 0.97 | (0.019) | [1429] | 0.94 | (0.011) | [80] |
| $\sigma_w$(d) | 1 | 0.93 | (0.013) | [125] | 0.98 | (0.014) | [731] | 0.95 | (0.013) | [48] |
| $\sigma_T$ | 1 | 0.98 | (0.042) | | 1.01 | (0.031) | | 1.02 | (0.032) | |
| $\sigma_T$(d) | 1 | 0.94 | (0.084) | | 1.00 | (0.034) | | 1.06 | (0.125) | |
| $\overline{u_3'u_1'}$ | 1 | 0.84 | (0.015) | | | N/A | | 1.07 | (0.008) | |
| $\overline{u_3'u_1'}$(d) | 1 | 0.84 | (0.013) | | | N/A | | 1.09 | (0.009) | |
| $\overline{u_3'T'}$ | 1 | 0.89 | (0.009) | | 0.96 | (0.019) | | 0.86 | (0.005) | |
| $\overline{u_3'T'}$(d) | 1 | 0.92 | (0.009) | | 0.92 | (0.019) | | 0.87 | (0.006) | |

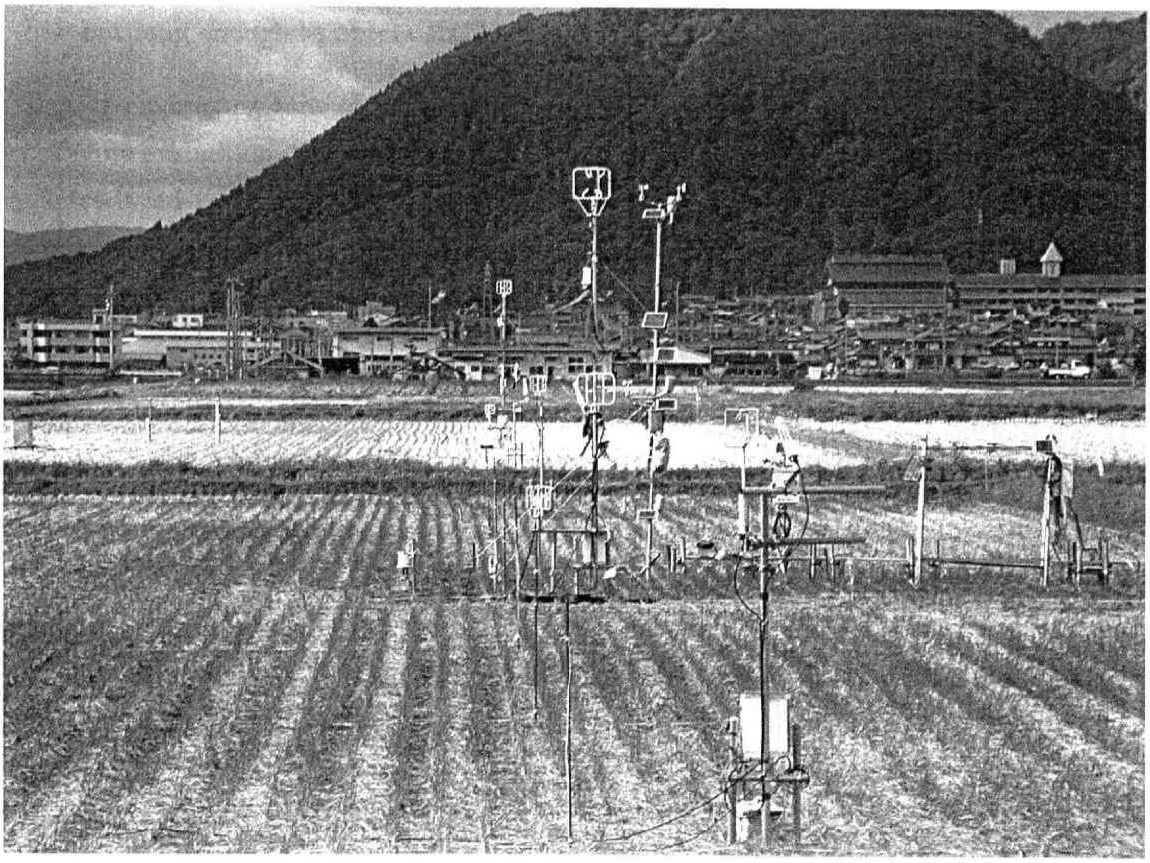

Photo3.1: Installed SATs in CAPS2003. A northward view from S1 site.

# Chapter 4

# Data Selection

## 4.1 Introduction

The main objective of this study is to evaluate each term and component of the TKE. In reality, the mean values of meteorological elements such as the wind speed, direction, air temperature change with time. Averaging time for evaluating each term of the TKE must be

- sufficiently short so that daily variations can be neglected,
- but long enough to obtain statistics.

Thus, the averaging time of the turbulence statistics is set to 10 min.

Before evaluation, the wind data must be adjusted with a new coordinate system such as introduced in Chapter 2. Further, the data must be also screened using thresholds of constancy and horizontal homogeneity. In this chapter, the methods of coordinate transformation and data selection are explained.

## 4.2 Transformations of Coordinate System

Since the averaging time is set to 10 min, the coordinate system is transformed every 10 min. In this section, the axis symbols $(x_1, x_2, x_3)$ are changed to $(x, y, z)$, and $(u_1, u_2, u_3) \Rightarrow (u, v, w)$ to avoid complexity. $x$ is the prevailing wind direction axis, $y$ is the horizontal direction axis orthogonal to $x$, and $z$ is the vertical direction axis.

The conceptual illustrations of the coordinate transformations are shown in Figure 4.1. The axis is rotated by the following procedure.

**Step 1:** The $\mathbf{x_0}$-axis is rotated to the mean horizontal wind vector $(\overline{\mathbf{u}})$ around the $\mathbf{z_0}$-axis (in the $\mathbf{x_0} - \mathbf{y_0}$ plane). The rotational angle is $\theta$, and the new coordinate system is $(\mathbf{x_1}, \mathbf{y_1}, \mathbf{z_0})$.

**Step 2:** Next, the $\mathbf{z_0}$-axis is rotated until $\overline{w} = 0$ around the $\mathbf{y_1}$-axis. The rotational angle is $\phi$, and the new coordinate system is $(\mathbf{x_2}, \mathbf{y_1}, \mathbf{z_1})$.

**Step 3:** Further, the $\mathbf{y_1}$-axis is rotated until the $\mathbf{z_1}$-axis is perpendicular to the stream surface ($\overline{v'w'} = 0$) around the $\mathbf{x_2}$-axis. The rotational angle is $\psi$, and the new coordinate system is $(\mathbf{x_2}, \mathbf{y_2}, \mathbf{z_2})$,

where

$$\psi = \frac{1}{2}\tan^{-1}\left(\frac{2\overline{v_1'w_1'}}{\overline{v_1'}^2 - \overline{w_1'}^2}\right). \tag{4.1}$$

For calculating the vertical turbulent flux, the coordinate system is usually transformed usually until Step 2. In fact, the sensible heat flux is calculated using the coordinate system of Step 2. The coordinate systems of Steps 2 and 3 show considerable difference above the complex terrain.

Let the angle between the $\mathbf{z_2}$-axis and $\mathbf{z_0}$-axis be $\gamma$,

$$\gamma = \frac{\sqrt{\sin(\psi^2)\cos(\phi^2) + \sin(\phi^2)}}{\cos\phi\cos\psi}. \tag{4.2}$$

When $|\gamma| \leq 10^\circ$, the calculated sensible heat flux using the coordinate system of Step 2 is correct (McMillen, 1988). Ishida (1995) compares the sensible heat fluxes that were calculated using these coordinate systems. The results show that a larger $\gamma$ value leads to a larger difference between the sensible heat fluxes calculated by the coordinate systems of Steps 2 and 3. Only the data that satisfy the condition of $|\gamma| \leq 10^\circ$ are used in this study. Further, the data of Step 3 –$\mathbf{x_2} - \mathbf{y_2}$ plane is tangential to the stream surface– is used for the evaluation of the TKE terms. Since $\overline{v'w'} = 0$, the parameters related to the wind shear stress are much simpler. The friction velocity $u_*$ is

$$u_*^2 \equiv \sqrt{\overline{u'w'}^2 + \overline{v'w'}^2} = -\overline{u'w'}. \tag{4.3}$$

Moreover, the shear production term exists only in the $x(x_1)$-component (equations (2.7), (2.9)).

## 4.3 Homogeneity of the Data

The data used for the TKE evaluation must be screened in order to eliminate the temporal and spatial variations of the TKE and the horizontal strain of the wind environment. Hence, the following thresholds are used for the data screening.

### Constancy and Horizontal Homogeneity

Constancy and horizontal homogeneity –the conditions assumed for the TKE– can be applied to the evaluating of the TKE terms evaluation in Chapter 2 as follows

$$\frac{\partial R_{ii}}{\partial t} = \overline{U_j}\frac{\partial R_{ii}}{\partial x_j} = 0. \tag{4.4}$$

However, there exist no data that are satisfied under these conditions. Thus, in this study, the following conditions are applied:

$$\frac{\left(\frac{\Delta q^2}{\Delta t}\right)}{q^2} \leq 0.1, \tag{4.5}$$

$$\frac{\max\left[|q_C^2 - q_{E1}^2|, |q_C^2 - q_{S1}^2|, |q_{S1}^2 - q_{E1}^2|\right]}{q^2} \leq 0.1. \tag{4.6}$$

where $q^2 \equiv \overline{u_i'^2}$ is the average TKE at C ($q_C^2$), E1 ($q_{E1}^2$), and S1 ($q_{S1}^2$) sites, and $\Delta t$ is set to 10 min. Equations (4.5) and (4.6) represent the constancy and horizontal homogeneity limitations, respectively.

### Stability of Wind Direction

The coordinate transformations described in Section 4.2 are performed under the assumption that the wind direction is constant during the averaging time (10 min). In reality, the wind direction is not constant. Here, the stability of the wind direction is defined as $|\overline{\mathbf{u}_{10\mathrm{min}}}|/\overline{|\mathbf{u}_{10\mathrm{min}}|}$ $(= 0 \sim 1)$ in this study. The numerator is a vector-averaged absolute wind speed, while the denominator is a scalar-averaged wind speed. When the wind direction is constant for an averaging time, this value is 1. In this study, the threshold is given as

$$\frac{|\overline{\mathbf{u}_{10\mathrm{min}}}|}{\overline{|\mathbf{u}_{10\mathrm{min}}|}} > 0.8. \tag{4.7}$$

### Horizontal Momentum Flux

$\overline{u_1' u_2'}$ is the horizontal momentum flux, which transports the turbulent momentum $u_1'$ in the $x_2$-direction or $u_2'$ in the $x_1$-direction. This momentum flux is significantly larger if exhibit horizontal heterogeneity of the wind speed. Conversely, sufficiently small horizontal momentum flux suggests the homogeneity of the horizontal wind. The threshold is proposed as

$$\left|\frac{\overline{u_1' u_2'}}{\overline{u_1'^2}}\right| < 0.087, \tag{4.8}$$

where 0.087 corresponds to $\tan 5^\circ$.

## 4.4 Concluding Remarks

In order to eliminate the temporal and spatial variations of the TKE and the horizontal strain (shear) of the wind environment, the coordinate system is transformed in 3 steps; further, the data for evaluating each term of the TKE are limited. After the data are selected, 8.4% of the total data (369/4380) remains.

The limitation conditions related to horizontal homogeneity described in this chapter are original. This is probably why the results are different from those of conventional studies, particularly with regard to the horizontal components. In Chapter 6, the selected data are used for evaluation in Chapter 6.

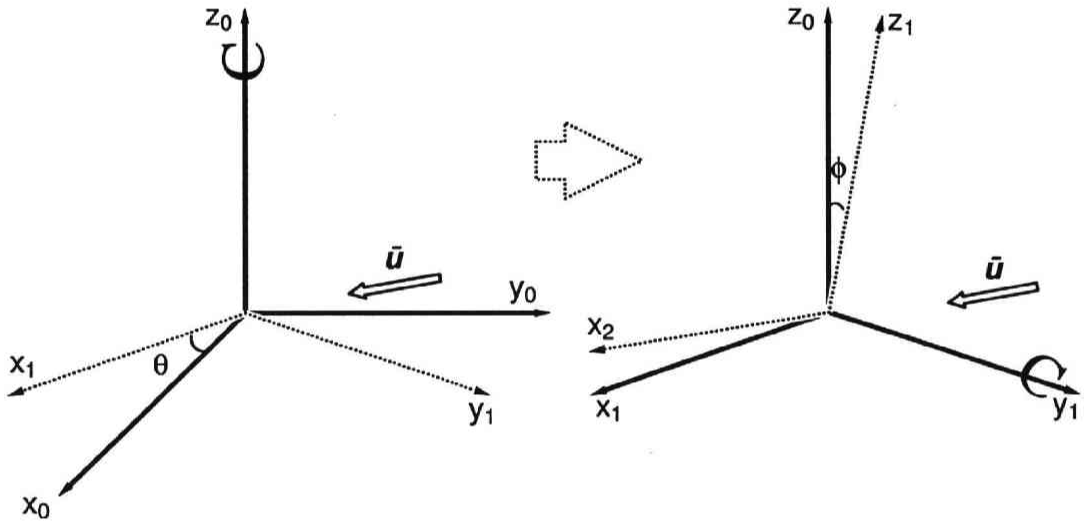


Figure 4.1: Conceptual illustrations of coordinate transformations. (Left panel) Step 1, (Right panel) Step 2.

# Chapter 5

# Normality of Third- and Fourth-order Moments

## 5.1 Introduction

In order to completely simulate a turbulent environment, a large number of unknowns need to be solved in the equations (see Section 2.4). However, since the number of unknowns is larger than the number of equations, it is important to parameterize the higher-order moments with the lower-order ones. This is referred to as the turbulent closure problem. This problem arises due to the nonlinear characteristics of fluid dynamics. In this chapter, parameterizations of third- and fourth-order moments with second-order moments are discussed by using field data.

Since turbulence is apparently a random motion, a quasi-normal distribution hypothesis was adopted. If the PDF of the turbulence has a normal distribution, the parameterizations of the turbulence are greatly simplified; all the third-order moments equal 0, and the fourth-order moments can be represented by a summation of second-order moment products. Although the turbulence tends to be isotropic and random in the absence of an external force, the PDF of the turbulence is not exactly normal because of external forces that produce the turbulence. Examples of these external forces are friction and buoyant forces generated at the Earth's surface. Some studies have been the third- and fourth-order moments in order to understand the vertical structure of convection in the atmospheric boundary layer. Alberghi et al. (2002) shows the relationship between skewness and kurtosis of the vertical wind speed $u_3$ by using SODAR data. Gryanik and Hartmann (2002) show the parameterization of the third- and fourth-order moments that are related to the vertical wind speed $u_3$ and the potential temperature $\theta$ by using aircraft data. The objective of this chapter is the parameterization of the third- and fourth-order moments of wind speed in the surface boundary layer.

## 5.2 Skewness and Kurtosis

Skewness and kurtosis are statistical parameters. Skewness is a measure of the asymmetry of the probability distribution of a random variable. This is a third-order normalized moment and is written as

$$\mathrm{Sk} \equiv \frac{\sum_{i=1}^{N}(x_i - \overline{x})^3}{\left(\sum_{i=1}^{N}(x_i - \overline{x})^2\right)^{3/2}} = \frac{\overline{x_i'^3}}{\sigma_x^3}. \tag{5.1}$$

The denominator is a cube of the standard deviation, and the numerator is a third-order moment. The distribution has a positive skew (right-skewed) if the higher tail is longer and a negative skew (left-skewed) if the lower tail is longer.

On the other hand, kurtosis is a measure of the peakedness of the probability distribution of a real-valued random variable. Kurtosis is the fourth-order normalized moment and is written as

$$\mathrm{Ku} \equiv \frac{\sum_{i=1}^{N}(x_i - \overline{x})^4}{\left(\sum_{i=1}^{N}(x_i - \overline{x})^2\right)^{2}} - 3 = \frac{\overline{x_i'^4}}{\sigma_x^4} - 3. \tag{5.2}$$

The denominator is the fourth power of the standard deviation, and the numerator is a fourth-order moment. The $-3$ at the end of this formula is often explained as a correction to make the kurtosis of the normal distribution equal to zero. A positive kurtosis implies that a greater proportion of the variance is due to infrequent extreme deviations rather than frequent modestly-sized deviations.

In order to close the second-order equations of turbulence, unknown third-order moments are required; further third-order moments require fourth-order moments. On the other hand, if the probability distribution of the turbulence is assumed to be a normal Gaussian distribution, the third-order moments are equal to 0, and the fourth-order moments can be expressed as a summation of the second-order moments

$$\frac{\overline{u_i' u_j' u_k' u_l'}}{u_*^4} = r_{ij}r_{kl} + r_{ik}r_{jl} + r_{il}r_{jk}, \tag{5.3}$$

where $i \sim l$ independently take values from $1 \sim 3$ and do not represent Einstein's summation in this case. For the simple case of $i = j = k = l$, the third-order and fourth-order moments normalized by friction velocity are expressed as

$$r_{iii} = \frac{\overline{u_i'^3}}{u_*^3} = 0, \tag{5.4}$$

$$r_{iiii} = \frac{\overline{u_i'^4}}{u_*^4} = 3r_{ii}^2. \tag{5.5}$$

The deviations from equations (5.4) and (5.5) are similar to those for skewness and kurtosis in statistics, respectively. In this study, kurtosis is defined in an expanded sense as

$$\mathrm{Ku} \equiv \frac{r_{ijkl}}{r_{ij}r_{kl} + r_{ik}r_{jl} + r_{il}r_{jk}} - 3. \tag{5.6}$$

Monin and Yaglom (1971) state that the fourth-order moments can be approximated as quasi-normal even if the third-order moments are not zero. These relations are termed as a quasi-normal distribution. In practice, the higher-order moments related to $u_3$ and $\theta_v$ are not normally distributed, and the fourth-order moments correlate with the third-order moments because of the surface existence (Alberghi et al., 2002; Gryanik and Hartmann, 2002). In the next section, some characteristics of the third- and fourth-order moments are discussed.

## 5.3 Third-order Moments

Firstly, all combinations of the third-order moments are calculated. The average and standard deviation values for all the valid data are shown in Table 5.1. All the absolute values of the averages exceed those of the standard deviations. This implies that the third-order moments spread around 0.

Further, on examining the stability dependencies of the third-order moments, no significant dependencies were found other than $r_{333}$. Examples of $r_{111}$ and $r_{222}$ are shown in Figure 5.1 and those of $r_{113}, r_{223}$, and $r_{333}$ are shown in Figure 6.3. Thus the normal distribution hypothesis of the third-order moments is to a certain extent with the exception of $r_{333}$. Wyngaard et al. (1971) shows the significant stability dependencies of $r_{113}, r_{223}$, and $r_{333}$. The differences in these results are discussed in Chapter 6.

## 5.4 Fourth-order Moments

Assuming a normal distribution, the fourth-order moments can be represented by the summation of the second-order moment products, as described in Section 5.2. Hence, the relationships between all combinations of the fourth-order moments and related second-order moments can be seen under unstable conditions (Table 5.2).

When $i = j = k = l$, the horizontal components ($i = 1, 2$) of turbulence show a normal distribution, whereas the distribution of the vertical component ($i = 3$) is significantly different from the normal distribution. Because of the intermittency of the plumes, the distribution of $u_3'$ is not Gaussian and the kurtosis is larger. Figure 5.2 shows the relationship between the second- and fourth-order moments for $i = j = k = l$ under

weakly unstable conditions. This difference is also clearly observed in this figure. Since the selected data are those with horizontal homogeneity (Chapter 4), the fourth-order moments related to $r_{12}$ and $r_{23}$ are small. In contrast to $r_{33}$, the fourth-order moments related to $r_{13}$ (but $r_{33}$); $r_{1113}$ and $r_{1223}$ take small values (kurtosis). This implies that there are few extreme deviations in $\overline{u_1' u_3'}$. $r_{1333}$ and $r_{1133}$ are related to both $r_{33}$ and $r_{13}$. Therefore, both the effects negate each other in these fourth-order moments, and these moments are normal as a result. $r_{1113}, r_{1133}$, and $r_{1333}$ are shown in Figure 5.3.

## 5.5 Concluding Remarks

The relationships among the second-, third-, and fourth-order moments are shown in this chapter. These results are related to the normality of the turbulence, and they can be used to resolve the turbulent closure problems.

The results of this chapter can be summarized as follows:

- The normal distribution hypothesis can be applied to the higher-order moments of $u_1'$ and $u_2'$.
- On the basis of the skewness and kurtosis values of $u_3'$ ($\mathrm{Sk} > 0, \mathrm{Ku} > 0$), it can be concluded that $u_3'$ has an extremely large positive value.
- However, most values of $\overline{u_1' u_3'}$ are distributed near the average.

These results indicate the intermittency of the plumes under unstable conditions. However, such a tendency is not seen in the Reynolds stress $\overline{u_1' u_3'}$ for a vertical momentum flux. This is probably because the surface of the observational site is relatively flat. The tendency of $\overline{u_1' u_3'}$ on a rough surface might differ.

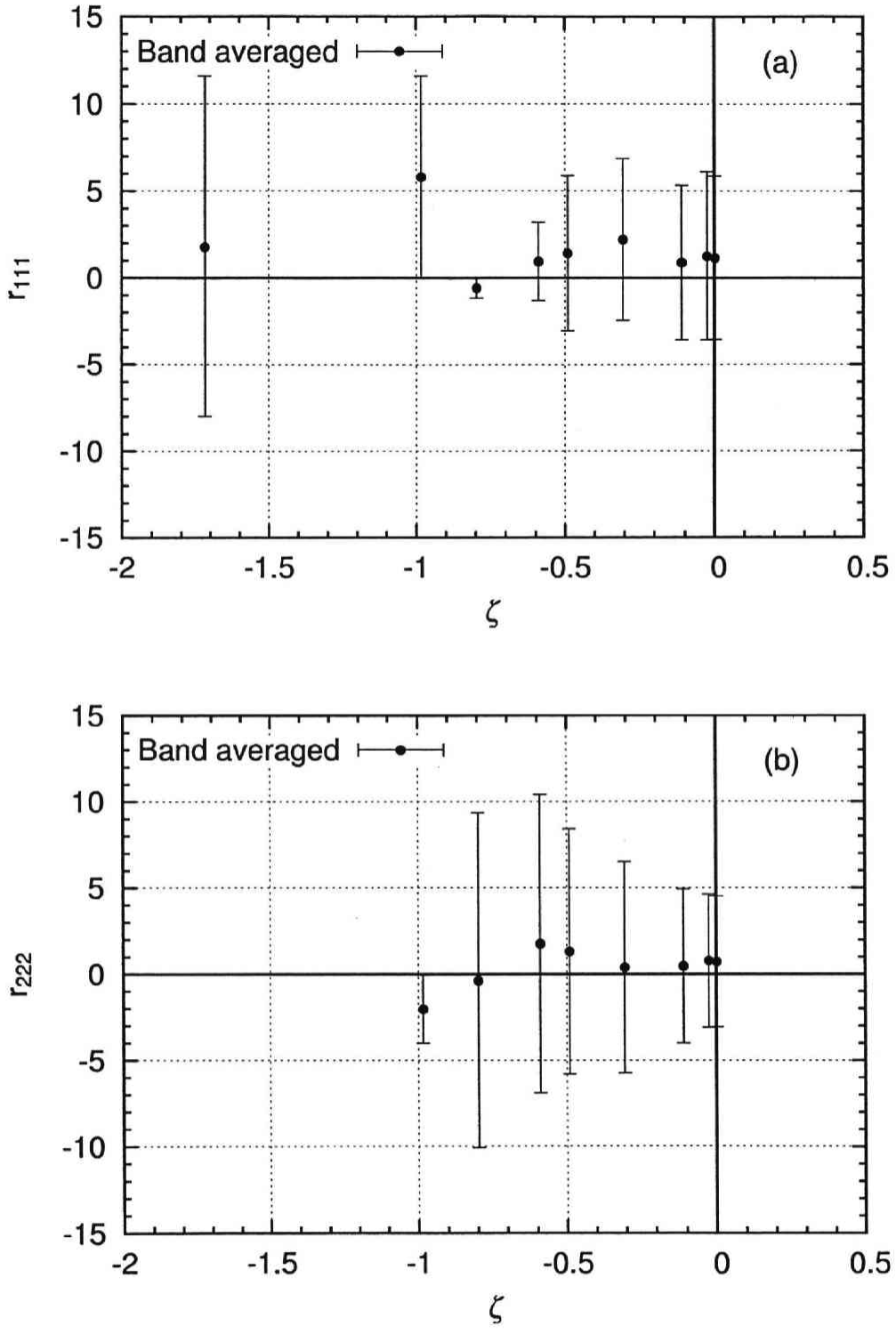


Figure 5.1: Relationship between the normalized third-order moments $r_{iii} = \overline{u_i'^3}/u_*^3$ and the Obukhov length $\zeta$. (a) $r_{111}$, (b) $r_{222}$. $r_{333}$ is shown in Figure 6.3.

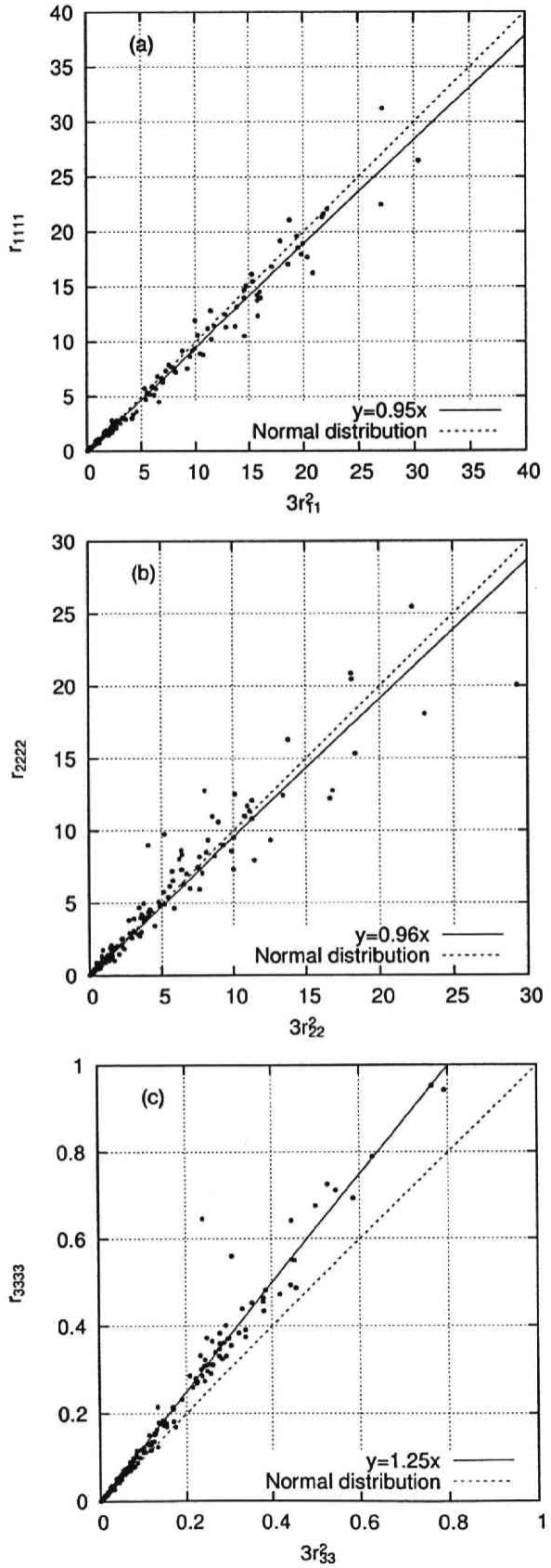


Figure 5.2: Relationships between the normalized second and fourth-order moments ($-1 < \zeta < 0$). $r_{iiii} = \overline{u_i'^4}/u_*^4$, $r_{ii} = \overline{u_i'^2}/u_*^2$. (a)$r_{1111}$, (b)$r_{2222}$, (c)$r_{3333}$.

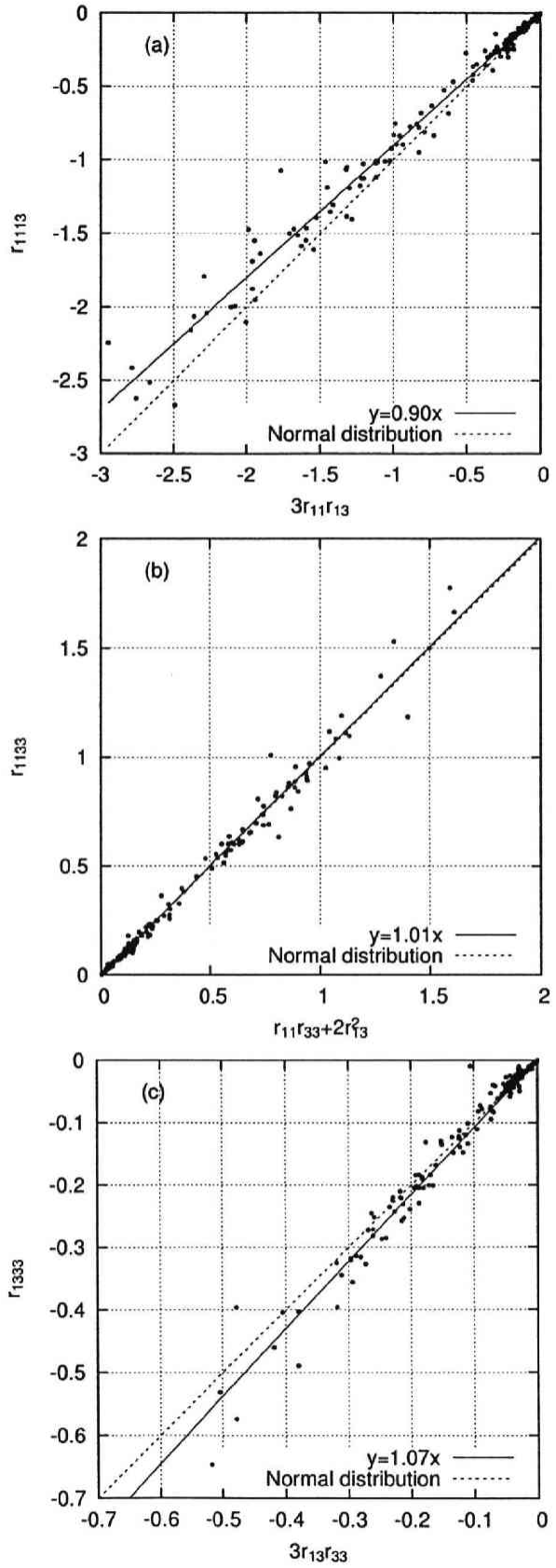


Figure 5.3: Relationships between the normalized second and fourth-order moments ($-1 < \zeta < 0$). $r_{ijkl} = \overline{u'_i u'_j u'_k u'_l}/u_*^4$, $r_{ij} = \overline{u'_i u'_j}/u_*^2$. (a)$r_{1113}$, (b)$r_{1133}$, (c)$r_{1333}$.

Table 5.1: Averages and standard deviations of the normalized third-order moments for all combinations ($-2.0 < \zeta < 0.5$). $r_{ijk} = \overline{u_i' u_j' u_k'}/u_*^3$. Under a condition of normal distribution, $\overline{r_{ijk}} = \mathrm{Sk} = 0$.

| 3rd-order moments | Average | S.D. ($\sigma$) |
|---|---|---|
| $^{*}r_{111}$ | 1.8 | 4.8 |
| $r_{112}$ | 1.0 | 4.7 |
| $^{**}r_{113}$ | −0.3 | 2.5 |
| $r_{122}$ | 1.3 | 3.2 |
| $r_{123}$ | 0.2 | 3.9 |
| $r_{133}$ | 0.6 | 3.0 |
| $^{*}r_{222}$ | 0.7 | 3.4 |
| $^{**}r_{223}$ | 0.2 | 1.9 |
| $r_{233}$ | 1.5 | 3.1 |
| $^{**}r_{333}$ | −0.2 | 1.9 |

*: shown in Figure 5.1; **: shown in Figure 6.3.

Table 5.2: Relationships between the normalized fourth-order and related second-order moments for all combinations ($-1 < \zeta < 0$). $r_{ijkl} = \overline{u'_i u'_j u'_k u'_l}/u_*^4$, $r_{ij} = \overline{u'_i u'_j}/u_*^2$. Under a condition of normal distribution, $\overline{r_{ijkl}/\sum r_{ij}} = 1$, and kurtosis (Ku) equals to 0.

| 4th-order moments | Related 2nd-order moments | $\overline{r_{ijkl}}$ | $\overline{r_{ijkl}/\sum r_{ij}}$ | Ku |
|---|---|---|---|---|
| $^{*}r_{1111}$ | $3r_{11}^2$ | 5.52 | 0.95 | −0.15 |
| $r_{1112}$ | $3r_{11}r_{12}$ | 0.02 | 1.02 | 0.06 |
| $^{**}r_{1113}$ | $3r_{11}r_{13}$ | −0.59 | 0.90 | −0.30 |
| $r_{1122}$ | $r_{11}r_{22} + 2r_{12}^2$ | 1.67 | 1.08 | 0.24 |
| $r_{1123}$ | $r_{11}r_{23} + 2r_{12}r_{13}$ | $10^{-3}$ | — | —$^{\sharp}$ |
| $^{**}r_{1133}$ | $r_{11}r_{33} + 2r_{13}^2$ | 0.36 | 1.01 | 0.03 |
| $r_{1222}$ | $3r_{12}r_{22}$ | −0.04 | — | —$^{\sharp}$ |
| $r_{1223}$ | $r_{13}r_{22} + 2r_{12}r_{23}$ | −0.16 | 0.92 | −0.24 |
| $r_{1233}$ | $r_{12}r_{33} + 2r_{13}r_{23}$ | $10^{-4}$ | — | —$^{\sharp}$ |
| $^{**}r_{1333}$ | $3r_{13}r_{33}$ | −0.11 | 1.07 | 0.21 |
| $^{*}r_{2222}$ | $3r_{22}^2$ | 4.49 | 0.96 | −0.12 |
| $r_{2223}$ | $3r_{22}r_{23}$ | 0.01 | — | —$^{\sharp}$ |
| $r_{2233}$ | $r_{22}r_{33} + 2r_{23}^2$ | 0.29 | 1.13 | 0.39 |
| $r_{2333}$ | $3r_{23}r_{33}$ | $10^{-3}$ | — | —$^{\sharp}$ |
| $^{*}r_{3333}$ | $3r_{33}^2$ | 0.19 | 1.25 | 0.75 |

*: shown in Figure 5.2; **: shown in Figure 5.3; $^{\sharp}$: not significant.

# Chapter 6

# Evaluation of Each Term of TKE Equations

## 6.1 Introduction

Turbulent kinetic energy (TKE) is one of the most fundamental variables in the atmospheric boundary layer (ABL), and its budgets are important for demonstrating the physical processes in turbulent fluid motions. Each term of the TKE equation was evaluated by Wyngaard and Côté (1971) using the 1968 Kansas experiment data. To date, many researchers have attempted to evaluate these terms by field or numerical experiments. Because of the difficulty in performing such measurements and the requirement of surface homogeneity, these terms were typically not evaluated directly but were parameterized with higher-order moments. Further, it is difficult to measure the ABL pressure fluctuation. Thus, pressure derivatives are evaluated as residuals. Recently, a few experiments (Wyngaard et al., 1994; Cuxart et al., 2002) and large-eddy simulations (Dwyer et al., 1997; Skyllingstad, 2003; Miles et al., 2004) were carried out; however, their results were not comprehensive.

In this chapter, each component and term of TKE equations for the lowest surface boundary layer is evaluated using the screened data (Chapter 4). However, the pressure correlation terms are evaluated as the residual of the other terms measured accurately.

The TKE equation is usually treated as the summation of each component, and only the vertical component of the pressure correlation term is expressed conventionally. While the total pressure correlation term have been considered as zero, the individual components are not necessarily zero and should redistribute the TKE isotropically beyond the components. Because each component of the TKE budget is closed. The characteristics and functions of the pressure correlation terms are also discussed.

## 6.2 Shear Production

The normalized shear production term is equal to the wind shear function $\phi_M$ expressed by equation (2.8). After the data screening, most of the remaining data are valid for $-1 < \zeta < 0.5$ (e.g. Figure 6.6). Thus, the following conventional relationships, covering large $\zeta$ ranges, are used.

The wind shear function under unstable conditions ($0 > \zeta > -1$) was determined by Dyer and Hicks (1970). Under stable conditions, the wind shear function of Kondo et al. (1978) was used,

$$\phi_M(\zeta) = \begin{cases} (1-16\zeta)^{-\frac{1}{4}} & (\zeta < 0) \\ 1+7\zeta & (\zeta > 0). \end{cases} \tag{6.1}$$

Kondo and Ishida (1997) confirmed that this function is applied to extremely unstable conditions ($\zeta > -477$) as follows. The shear function for heat is expressed in the same way as $\phi_M$ (equation (2.8)):

$$\phi_H(\zeta) = \frac{kz}{\theta_*}\frac{\partial \overline{T}}{\partial z}, \tag{6.2}$$

where $T$ is air temperature. The $\Psi$-function is an integral form of the $\phi$-function defined as:

$$\Psi = \int \phi(\zeta)\, d(\ln \zeta). \tag{6.3}$$

Then,

$$\Psi_M(\zeta) = \frac{k}{u_*}U(z), \tag{6.4}$$

$$\Psi_H(\zeta) = \frac{k}{\theta_*}\left(T_S - T(z)\right), \tag{6.5}$$

where $\theta_*$ is friction velocity. Brutsaert (1992) expressed the shear function for heat when $-0.01 > \zeta > -20$ as

$$\phi_H(\zeta) = \frac{0.33 + 0.057y^{0.78}}{0.33 + y^{0.78}}. \tag{6.6}$$

Integration of equations (6.1), (6.6) leads to

$$\Psi_M = \ln\frac{z}{z_0} + \ln\frac{({x_0}^2+1)(x_0+1)^2}{(x^2+1)(x+1)^2} + 2(\tan^{-1}x - \tan^{-1}x_0), \tag{6.7}$$

$$\Psi_H = \ln\frac{z}{z_T} + 1.2\ln\frac{0.33 + {y_T}^{0.78}}{0.33 + y^{0.78}}, \tag{6.8}$$

where

$$x = (1-16\zeta)^{\frac{1}{4}}, x_0 = (1-16\zeta_0)^{\frac{1}{4}}, x_T = (1-16\zeta_T)^{\frac{1}{4}},$$

$$y = -\zeta, \qquad y_T = -\zeta_T,$$

$$\zeta_0 = \frac{z_0}{L}, \qquad \zeta_T = \frac{z_T}{L}.$$

Here, $z_0$ and $z_T$ are the roughness lengths for the wind and temperature profiles, respectively.

Several comparisons are made between the sensible heat flux $H_{eddy} = c_P\rho\overline{u_3'\theta_v'}$ calculated by eddy correlation method, and those estimated $H_p = c_P\rho u_*\theta_*$ using the $\Psi$-functions (profile method). Using the roughness lengths of $z_0$ and $z_T$ measured under windy conditions, the observed values of $U(z)$, $T(z)$, and the $\Psi$-functions, the estimated sensible heat $H_p$ can be evaluated by successive approximations, by use of equations (6.4) and (6.5). The initial values of $u_*$ and $T_*$ are determined by use of equations (6.4), (6.5) and $\Psi$-functions under neutral conditions as $\Psi_M = \ln(z/z_0)$ and $\Psi_H = \ln(z/z_T)$. Making use of equations (6.7) and (6.8) will also yield estimated values of $H_p$. Figure 6.1 shows comparisons between the observed values of $H_{eddy}$ and the estimated $H_p$ values. Plotted data are distinguished by the symbols (see the figure legend) according to the value of $\zeta = z/L$. It can be seen that the $\Psi$-functions given by equations (6.7) and (6.8) produces good estimation values under strongly unstable conditions. Therefore, $\phi_M$-function of upper term of equation (6.1) is valid for $(0 < \zeta < -477)$.

## 6.3 Turbulent Transport

In order to estimate the turbulent transport term directly, it is necessary to measure the vertical gradient of the third-order moment. However, since the sensors are installed at only three different heights. The resolution of height is insufficient, and besides, the complete three height profile data set is limited. Under unstable conditions ($\zeta < 0$), the difference between three heights of $r_{333} = \overline{u_3'^3}/u_*^3$ by using this data set is shown in Figure 6.2. Although $\partial r_{333}/\partial x_3$ seems to be positive, the number of data is very limited.

Therefore, another estimating method is required. As described by Wyngaard and Côté (1971), the turbulent transport term is estimated as a function of the stability $\zeta$,

$$-\frac{kx_3}{2u_*^3}\frac{\partial\overline{u_i'^2u_3'}}{\partial x_3} = -\frac{k\zeta}{2}\frac{\partial r_{ii3}}{\partial\zeta}. \tag{6.9}$$

Figure 6.3 shows the relationship between the normalized third-order moment $r_{ii3}$ and $\zeta$. While the horizontal third-order moments $r_{113}, r_{223}$ are largely scattered around 0, the vertical moment $r_{333}$ increases consistently with $\zeta$ by using the screened data (Chapter 4). Under stable conditions, $r_{ii3} = 0$. It is significantly different from that of Wyngaard and Côté (1971), in which the horizontal components $r_{113}, r_{223}$ have larger positive values. Since $r_{113} + r_{223}$ calculated using unscreened (Equation (4.8)), double axis rotation ($\overline{u_2'u_3'} \neq 0$) data is significantly positive (Figure 6.4), the data screening and the third axis rotation processes must eliminate the horizontally skewed data.

Based on rough estimation, $r_{113}, r_{223} \simeq 0$ and $r_{333} = -1.7\zeta$. Thus, the turbulent transform term is expressed as follows:

$$\begin{aligned} -\frac{kx_3}{2u_*^3}\frac{\partial \overline{u_1'^2 u_3'}}{\partial x_3} &= 0, \\ -\frac{kx_3}{2u_*^3}\frac{\partial \overline{u_2'^2 u_3'}}{\partial x_3} &= 0, \\ -\frac{kx_3}{2u_*^3}\frac{\partial \overline{u_3'^3}}{\partial x_3} &= 0.34\zeta. \end{aligned} \tag{6.10}$$

$r_{333}$ in Figure 6.3 is limited for $\zeta > -1.5$. $r_{333}$ calculated using the unscreened data is roughly same as (6.10) until strongly unstable conditions ($\zeta > -7$), but is much scattered (Figure 6.4).

## 6.4 Dissipation

In order to estimate the dissipation rate $\varepsilon$ directly, very accurate measurements are required for the Kolmogorov's micro scale $\eta = (\nu^3/\varepsilon)^{1/4}$($\simeq$1 mm); these measurements were not performed. Therefore, Kolmogorov's four-fifths law that uses only the structure function of $u_1$ without any empirical constants is used to estimate $\varepsilon$:

$$D_{u_1^3}(r) - 6\nu\frac{dD_{u_1^2}(r)}{dr} = -\frac{4}{5}\varepsilon r, \tag{6.11}$$

where the $n$-th order structure function $D_{u_1^n}(r) = \overline{[u_1(x_1+r) - u_1(x_1)]^n}$. By assuming the frozen turbulence hypothesis ($r = \overline{U_1}\tau$) and that the scale is limited in the inertial subrange ($r \gg \eta$), the following equation is obtained:

$$D_{u_1^3}(\tau) = \overline{[u_1(t+\tau) - u_1(t)]^3} = -\frac{4}{5}\varepsilon\overline{U_1}\tau, \tag{6.12}$$

where $\tau$ is time-lag.

In order to obtain sufficient quantity of data that includes the the inertial subrange, the data which was recorded at 50 Hz (C site; 1.25 and 2.50 m only) were used. 1-run period is set to 28 min. The mean dissipation rate is determined using the following procedure:

1. Calculate the third-order structure function $D_{u_1^3}(\tau)$ for the time-lag range of $\tau = 0.02 \sim 5$ sec.

2. Fit a linear regression model of the form $D_{u_1^3} = A\tau$ for the range of $\tau = 0.1 \sim 1$ sec. because most of the data has the inertial subrange in this time range.

3. Check if each fitting is correct (the inertial subrange exists).

4. Compute $\phi_\varepsilon$ from the slope $A$ using a function of

$$\phi_\varepsilon = -\frac{5kz}{4u_*^3}\frac{A}{\overline{U_1}}. \tag{6.13}$$

Figure 6.5 shows examples of determining the value of $A$. Good example shows clear inertial subrange. Such cases are usually seen in the daytime. So most of the normalized dissipation rate data are limited under unstable or neutral conditions.

There is another method to estimate the dissipation rate using the second-order structure function $D_{u_1^2}$ as:

$$D_{u_1^2}(\tau) = C_0\varepsilon\tau, \tag{6.14}$$

where $C_0$ is empirical constant. And Anfossi et al. (2000) pointed out that the value of $C_0$ varies 2.2–4.5. That is why this method is not applied in this study.

Figure 6.6 shows the relationship between the normalized dissipation term and the stability. The $\phi_\varepsilon$-function under unstable conditions given by Thiermann and Grassl (1992) is expressed as

$$\phi_\varepsilon = (1 - 3\zeta)^{-1} - \zeta,$$

and that given by Kanda et al. (2002) is expressed as

$$\phi_\varepsilon = (1 - 10.5\zeta)^{-1} - \zeta.$$

Although our data are in close agreement with that of Kanda et al. (2002), the function of Thiermann and Grassl (1992) fitted to rural data is adopted in this study, because the function of Kanda et al. (2002) is fitted to urban data. This would cause slightly different results of the pressure correlation terms under weakly unstable conditions. Since limited data is available for stable conditions, $\phi_\varepsilon$ is formulated so that this function is linear and continuous with that of Thiermann and Grassl (1992) at $\zeta = 0$,

$$\phi_\varepsilon = 1 + 2\zeta.$$

## 6.5 Pressure Correlation

The pressure correlation terms are estimated as the residuals of Equation (2.9). The stability dependencies of each and total terms of the TKE equation is shown in Figure 6.7. The total pressure correlation term is positive under unstable conditions, larger than the shear production term particularly when $\zeta < -2$, and negative under stable conditions. The TKE of the $x_2$-component is the energy received from the other components through this pressure correlation term because it does not contain any TKE source (shear or

buoyancy). The source is the $x_1$-component under stable to weakly unstable conditions. In contrast, the source is the $x_3$-component under unstable conditions.

Figure 6.8 describes the difference between each component of the TKE. It is very interesting that the $x_3$-component can be a source of the pressure correlation term under unstable conditions, although $x_1$ ($r_{11}$) is the largest component of the TKE. This result is quite different from the statement in conventional textbooks on the assumption of incompressible fluid (e.g. Garratt, 1992; p.36). The vertical strain generated by the buoyancy would be sufficiently large to provide the $x_2$-component with the TKE.

## 6.6 Concluding Remarks

Each term and component of the TKE equations are quantified using the field data: this confirms the temporal and spatial homogeneity using 16 SATs. The results are summarized as follows:

- The shear production and dissipation term is consistent with the conventional results.
- The turbulent transport term is considerably smaller than that of Wyngaard and Côté (1971). This is because the horizontal components are almost zero, although the vertical component is almost the same. This implies that the turbulence in the lowest surface boundary layer is skewed only in vertical direction. Data screening process probably eliminates the horizontally skewed data. Therefore, the difference between these results could be determined by data screening.
- The pressure correlation term is evaluated as the residual of the other terms (Figure 6.7). The total pressure correlation term gains the TKE under unstable conditions, and loses it under stable conditions. The results of each component indicate that this term redistributes the TKE isotropically from the $x_1, x_3$-component to the $x_2$-component. The source is the $x_1$-component under stable and weakly unstable conditions, and the $x_3$-component under unstable conditions.

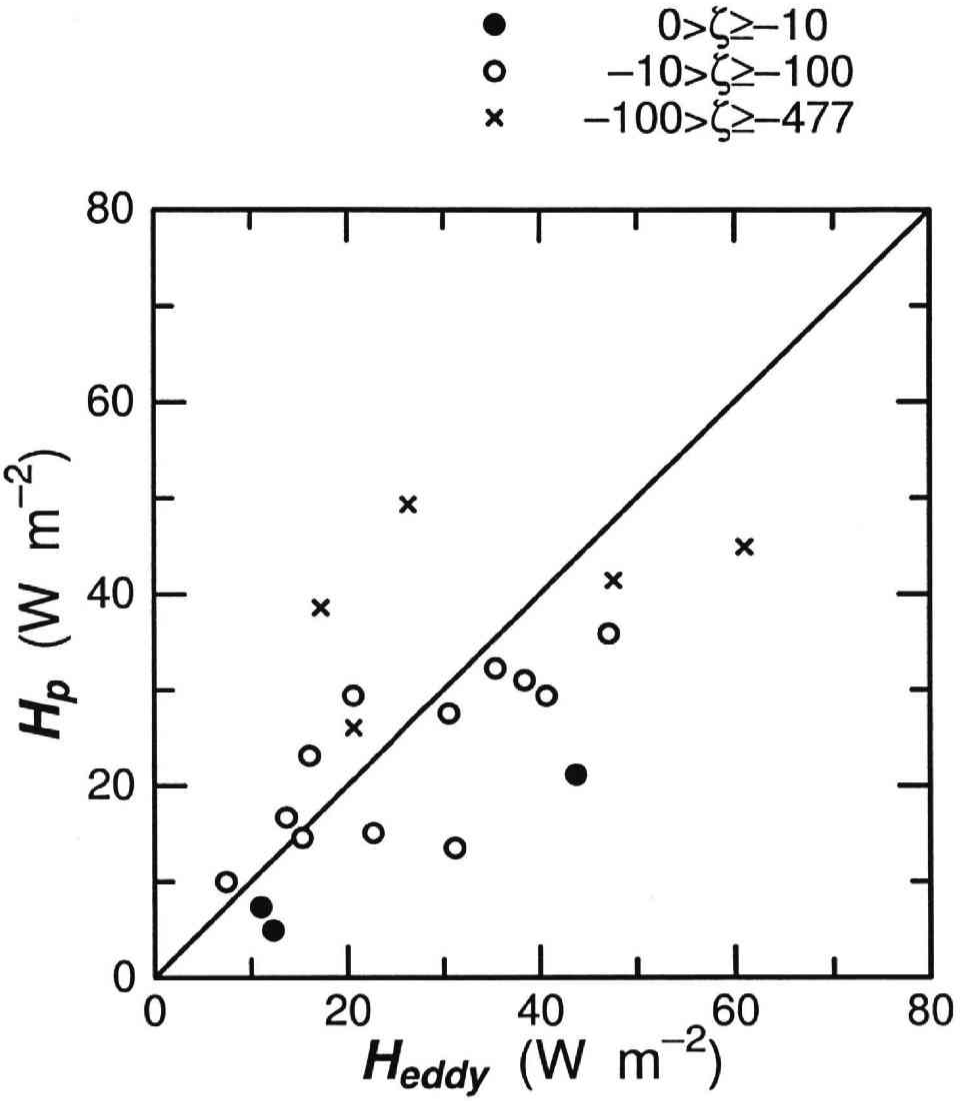


Figure 6.1: Comparison of calculated sensible heat fluxes under natural convective conditions. The ordinate value is calculated by the profile (gradient) method, the abscissa is by the eddy correlation method.

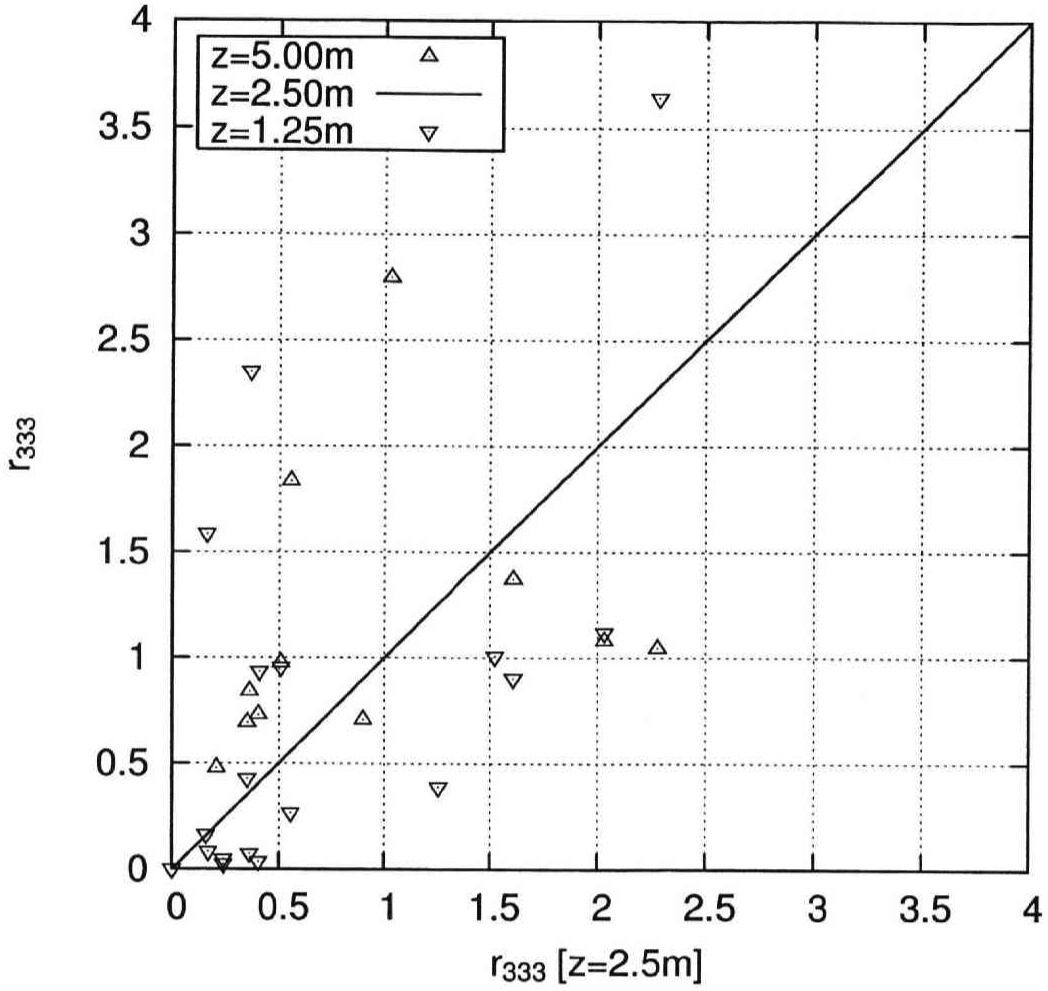


Figure 6.2: Height dependency of $r_{333} = \overline{u_3'^3}/u_*^3$ under unstable conditions ($\zeta \leq 0$). $\triangle : z = 5.00\text{m}$, $\nabla : z = 1.25\text{m}$

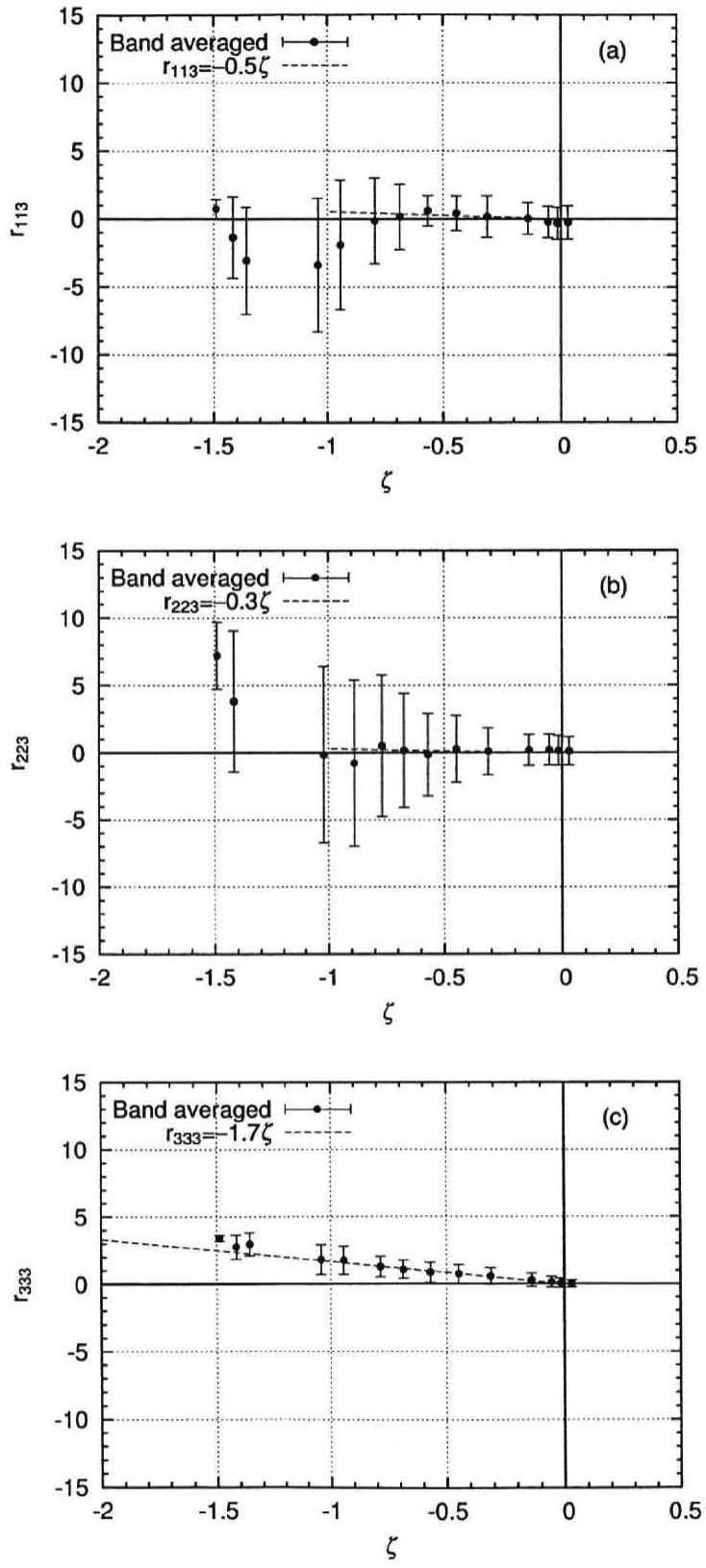


Figure 6.3: Relationship between the normalized third-order moments $r_{ii3} = \overline{u_i'^2 u_3'}/u_*^3$ and the Obukhov length $\zeta$. (a)$r_{113}$, (b)$r_{223}$, (c)$r_{333}$.

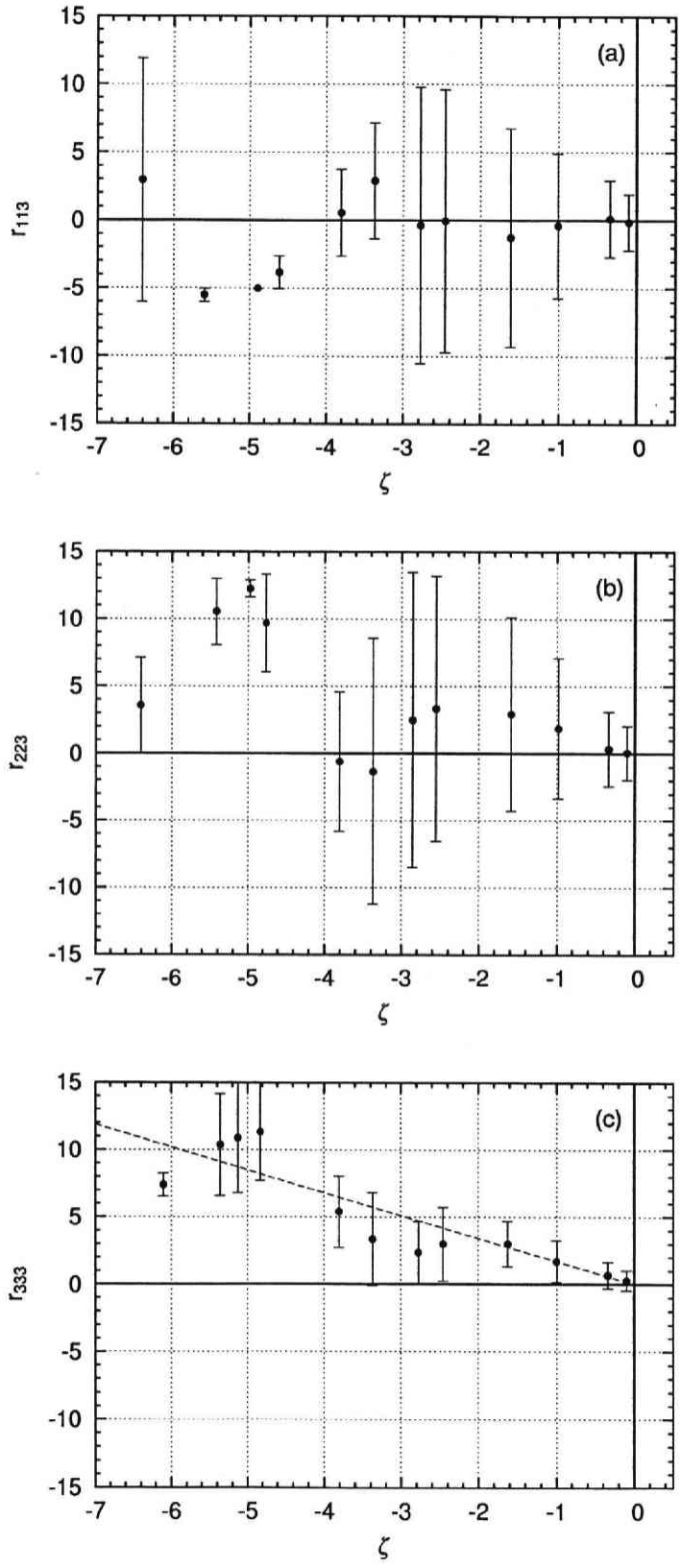


Figure 6.4: Same as Figure 6.3, but using unfiltered data. (a)$r_{113}$, (b)$r_{223}$, (c)$r_{333}$, broken line indicates $r_{333} = -1.7\zeta$ (see Figure 6.3).

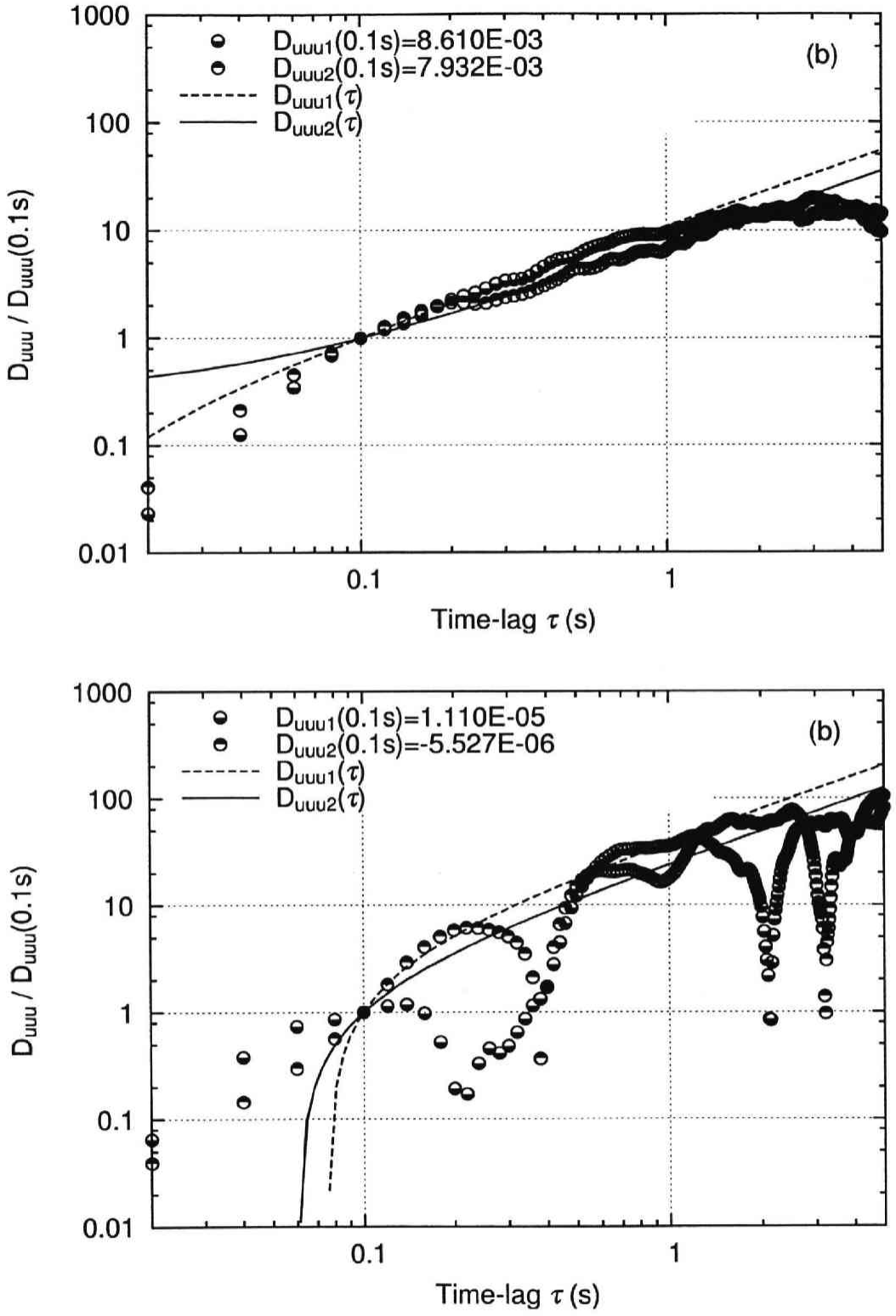


Figure 6.5: Relationships between the normalized third-order structure function $D_{uuu}/D_{uuu}(0.1s)$ and the time-lag $\tau$ at C site on October 5, CAPS2003. $D_{uuu1}$ is at $z = 1.25$m and $D_{uuu2}$ is at $z = 2.5$m. (a) succeeded example to fit (0930h JST; $L = -1.5$m, $\phi_\varepsilon \simeq 0.7$), (b) failed example to fit.

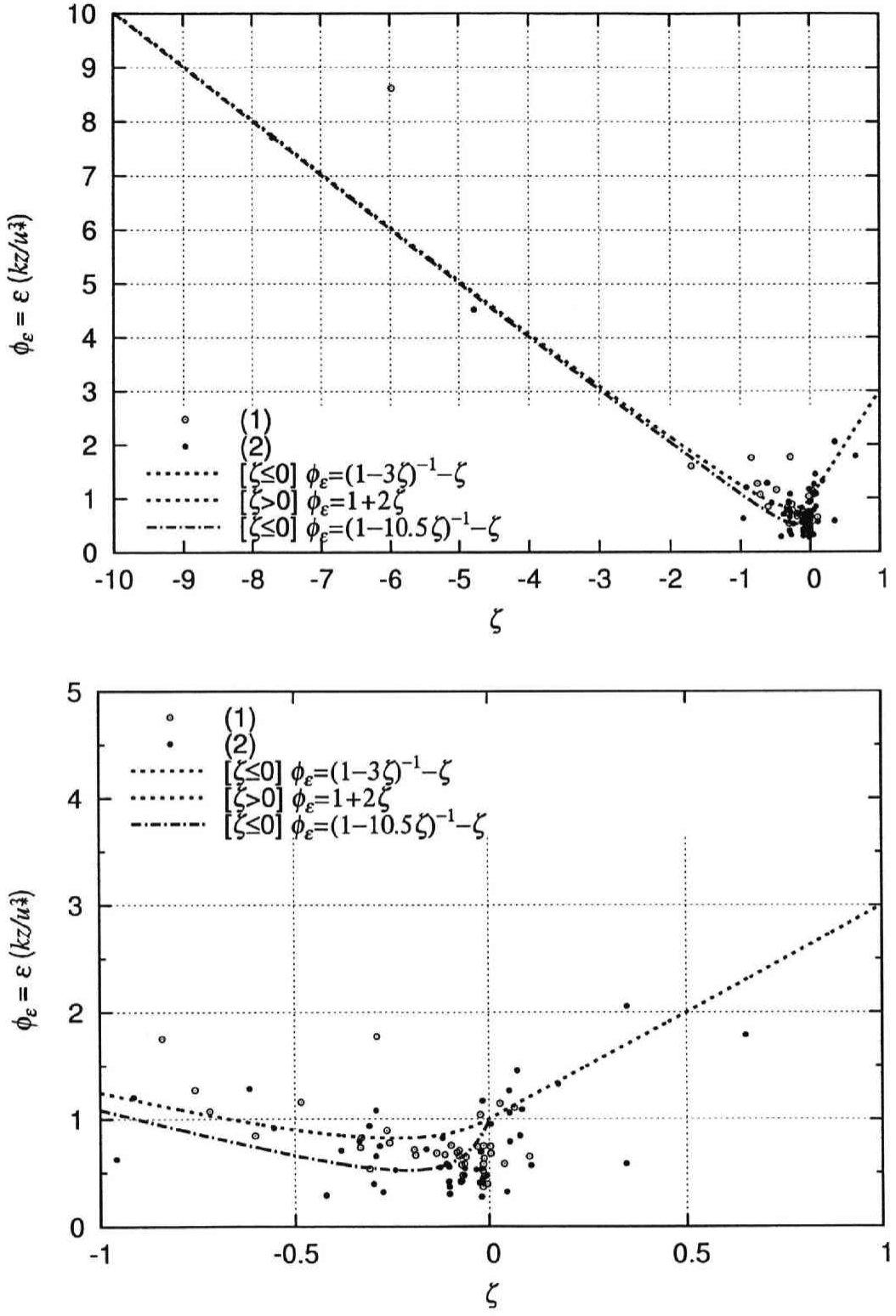


Figure 6.6: Relationship between the normalized dissipation term $\phi_\varepsilon = \varepsilon(kx_3/u_*^3)$ and the Obukhov length $\zeta$. The mark of ○ represents $z = 1.25$ m, • represents $z = 2.5$ m. (a) for $-10 < \zeta < 1$, (b) for $-1 < \zeta < 1$.

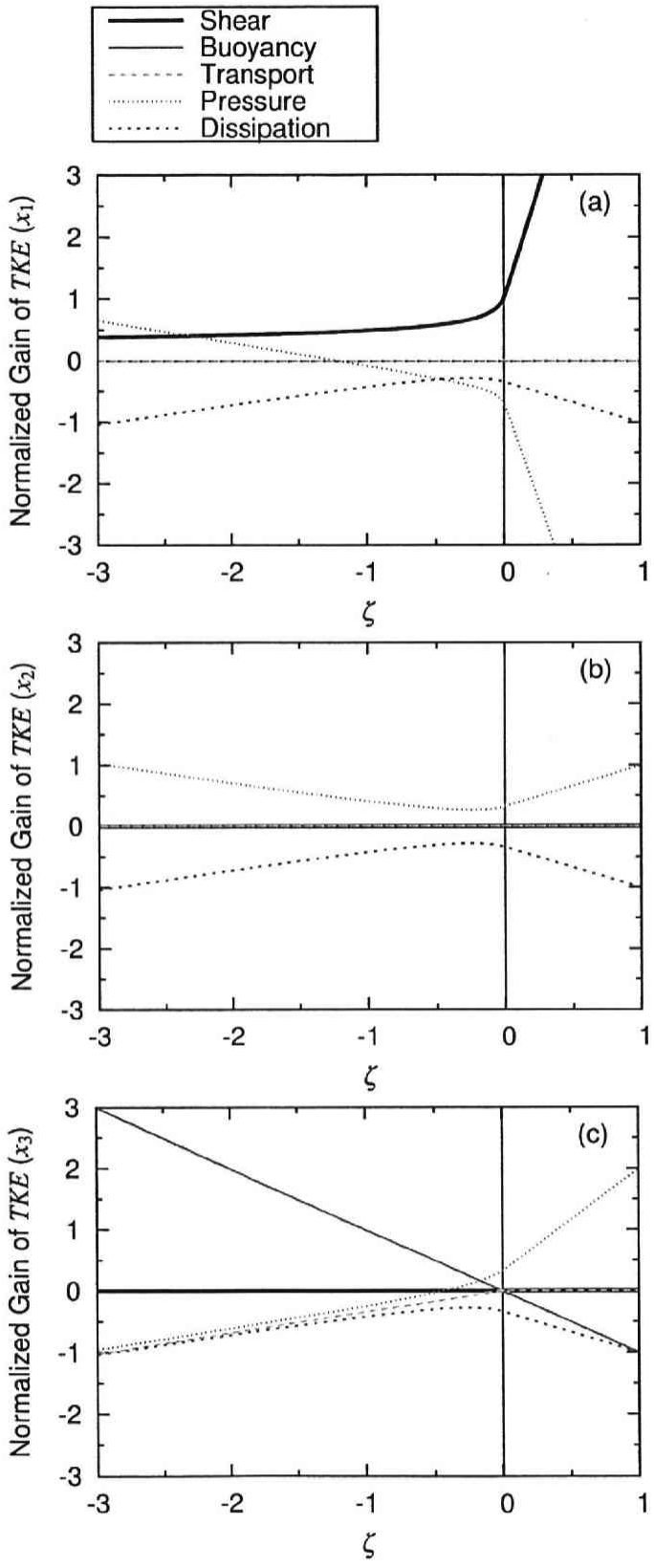


Figure 6.7: Stability dependency of each component and term of the TKE. (a) $x_1$, (b) $x_2$, (c) $x_3$-component.

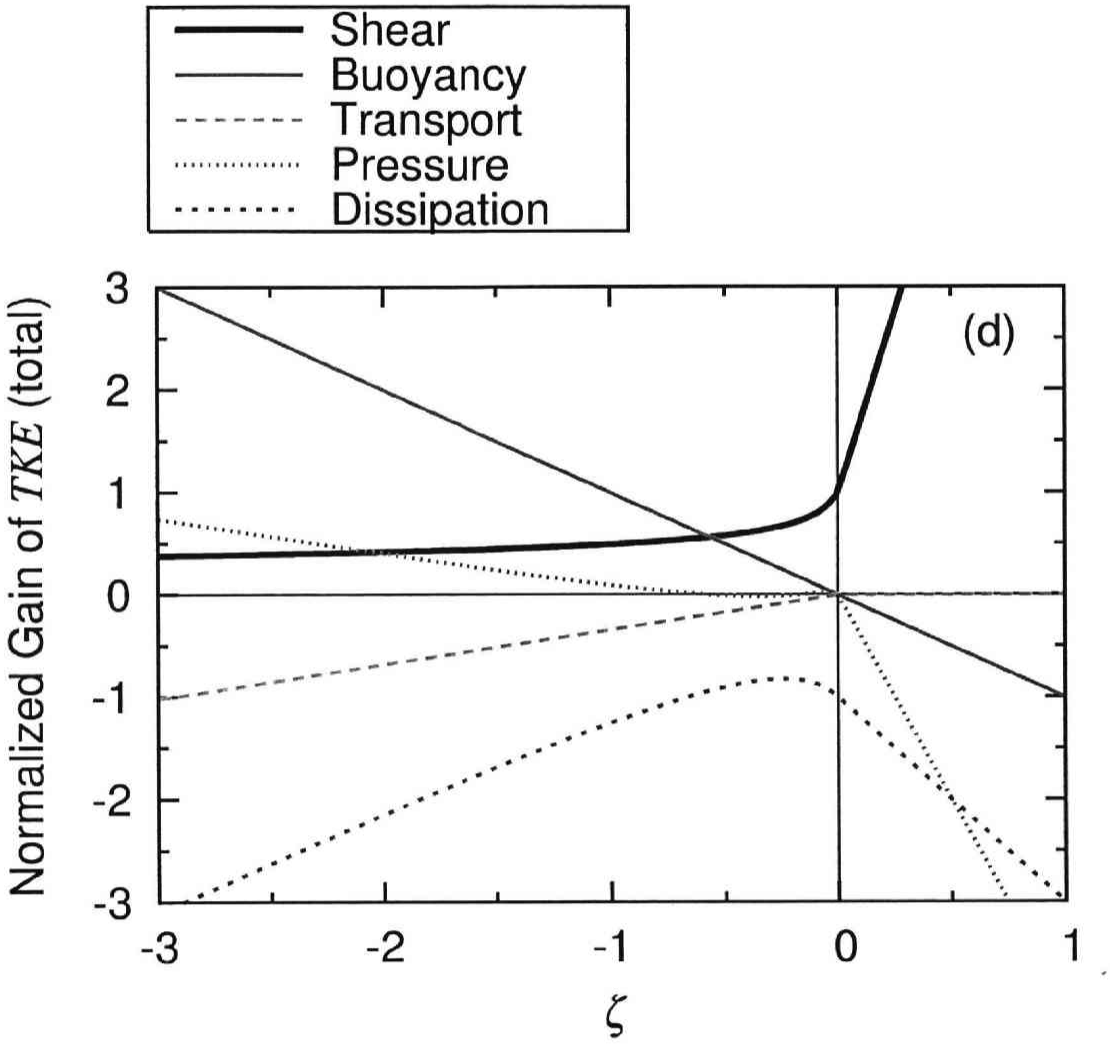


Figure 6.7: *continued.* (d) total TKE.

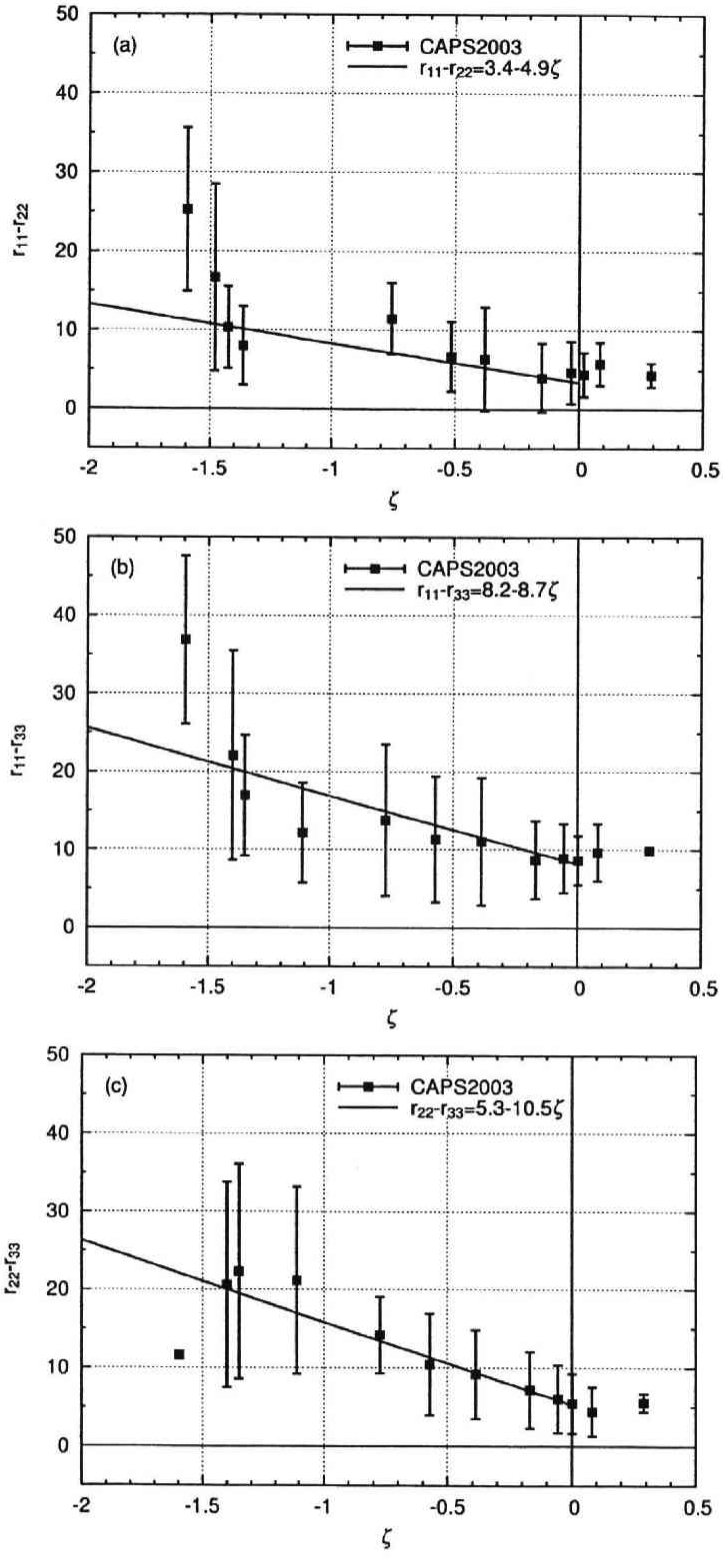


Figure 6.8: Relationship between the difference of each component of the normalized TKE $r_{ii} - r_{jj} = \left(\overline{u_i'^2} - \overline{u_j'^2}\right)/u_*^2$ and Obukhov length $\zeta$. (a) $r_{11} - r_{22}$, (b) $r_{11} - r_{33}$, (c) $r_{22} - r_{33}$.

# Chapter 7

# Sensible Heat Flux under Strongly Unstable Conditions

## 7.1 Introduction

The sensible heat flux under natural convective conditions, in which TKE is dominantly produced by the buoyancy, is one of the most important parameter to understand the mechanism of the convection. However, there have only been a few studies concerning the sensible heat flux under these conditions, due to the difficulty in observing the necessary meteorological elements. And a method for evaluating the flux under these conditions has not been properly established. For instance, the sensible heat flux $H$ is expressed by bulk formula as

$$H = c_P \rho C_H U (T_S - T), \tag{7.1}$$

where $c_P\rho$ is heat capacity of the air, $C_H$ is the bulk transfer coefficient for heat, and $U$ is scalar averaged wind speed. Under very calm ($U \to 0$) and convective conditions, the sensible heat flux is significantly positive. On the contrary, the sensible heat flux using equation (7.1) under such conditions is calculated too small because $U$ is meaningless. Thus, the exchange speed $C_H U$ is more useful.

Tropical atmospheric convection is a critical element in determining the earth's climate, as can be demonstrated by a well-known example, the El Niño – Southern Oscillation (ENSO) phenomenon. As part of the ENSO phenomenon, a so-called *warm pool* region exists in the western equatorial Pacific, characterized by high SSTs($> 27$ ℃) and low wind speeds over the entire year. Seager et al. (1988) pointed out that an SST change of 1 ℃ can be accomplished by a perturbation of only $12\,\mathrm{W\,m^{-2}}$ in the sensible heat flux from the warm pool. Yet an uncertainty on the order of $80\,\mathrm{W\,m^{-2}}$ is apparent in climatological estimates of the heat budget of the surface mixed layer in this region (Godfrey and Lindstorm, 1989; Weare, 1989).

In the urban area, the heat island phenomenon is a recent topic because urban thermal environment is getting worse. Air temperature of urban area is higher than rural

area because of less radiative cooling and larger sensible heat. Since the built-up urban structure prevent the ventilation, natural convective conditions frequently occur below the urban canopy. It is very important to evaluate the sensible heat flux, which affects urban air temperature, under such conditions. Sugawara (2001) attempts to evaluate the heat exchange between urban structure and the overlaying atmosphere based on observation and theoretical calculation.

In this chapter, an attempt is made to parameterize the sensible heat flux under natural convective conditions by analyzing indoor experiments and field observations. (Part of this chapter is cited by Kondo and Ishida, 1997.)

## 7.2 Exchange Speed of Sensible Heat under Natural Convective Conditions

On the basis of the Engineering of Heat Transfer, natural convection on an isothermal horizontal plate is treated by following non-dimensional parameters,

$$Nu = \frac{l}{\kappa} C_{\mathrm{H}} U \qquad \text{: Nusselt number,} \tag{7.2}$$

$$Gr = \frac{g\beta\, h^3 (T_{\mathrm{S}} - T)}{\nu^2} \qquad \text{: Grashof number,} \tag{7.3}$$

$$Pr = \frac{\nu}{\kappa} \qquad \text{: Prandtl number,} \tag{7.4}$$

and

$$Ra \equiv Gr \cdot Pr \qquad \text{: Rayleigh number.} \tag{7.5}$$

The parameter of $Nu$ denotes the non-dimensional exchange speed, while $Gr$ indicates the influence of convection due to buoyancy. Here, $l$ (m) is the scale length of the natural convection (e.g. the length of the surface or the size of the experimental convective cell), $\kappa$ ($\mathrm{m^2\,s^{-1}}$) the thermometric conductivity, $\nu$ ($\mathrm{m^2\,s^{-1}}$) the kinematic viscosity, and $\beta$ ($\mathrm{K^{-1}}$) the coefficient of thermal expansion.

From many experimental studies, it is well known that these parameters are related in natural convection as

$$Nu = A \cdot Ra^a. \tag{7.6}$$

Table 7.1 lists several numerical values of $A$ and $a$. Engineering studies have pointed out that an inclination of the test plate results in differences in the sensible heat flux. Mikheyev (1968) showed that the sensible heat flux on a horizontal plate is 1.3 times greater than that on a vertical plate. The results of Takeyama et al. (1983) shown in Table 7.1 have been corrected by this factor.

Since $a = 1/3$ for large value of $Ra$, (i.e. $8 \times 10^6 < Ra < 10^{13}$), $C_{\mathrm{H}}U$ can be described with use of the proportional constant $b$ as

$$\begin{aligned} C_{\mathrm{H}}U &\propto \frac{\kappa}{l} Ra^{\frac{1}{3}} \\ &\propto \frac{\kappa}{l} \left( \frac{g\beta l^3 (T_{\mathrm{S}} - T)}{\kappa\nu} \right)^{\frac{1}{3}} \\ &= b\,(T_{\mathrm{S}} - T)^{\frac{1}{3}} \qquad (\mathrm{m\,s^{-1}}), \end{aligned} \tag{7.7}$$

and then the sensible heat flux can be expressed as:

$$H = C(T_{\mathrm{S}} - T)^{\frac{4}{3}}. \tag{7.8}$$

It should be noted in equation (7.7) that $C_{\mathrm{H}}U$ does not depend on $l$. The value of $b$ has been estimated at 0.0013 to 0.0018 $\mathrm{m\,s^{-1}\,K^{-1/3}}$. For wet surface conditions, the buoyancy of the water vapor pressure difference should be taken into consideration.

Since engineering studies rely on indoor experiments, determination of $C_{\mathrm{H}}U$ for large values of $Ra$, or over a rough surface have not been researched in detail. In this study, the values of sensible heat flux for large $Ra$ ($> 10^{12}$) will be determined by indoor experiments, and confirmed by field observations.

## 7.3 Indoor Experiments

### 7.3.1 Smooth Surface

The indoor experiments were carried out with the use of readily available materials. Figure 7.1 is a conceptual illustration of the indoor experiment. The nearly constant temperature surface constructed of an aluminum plate with styrene foam is realized by exposition to solar radiation coming through the glass window. For the case of rough surface, aluminum cubes are distributed. Since the glass window cuts off longwave radiation from the outside atmosphere, and the wall temperatures in the experimental room have almost the same value as $T_{\mathrm{W}}$, the longwave radiation to the test surface is expressed by $\sigma {T_{\mathrm{W}}}^4$. Here, $\sigma$ ($= 5.67 \times 10^{-8}$ $\mathrm{W\,m^{-2}\,K^{-4}}$) is the Stefan–Boltzmann constant, and $T_{\mathrm{W}}$ the effective infrared temperature of the walls. The value of $T_{\mathrm{W}}$ is obtained from the average temperature of the walls and ceiling as observed by an infrared thermometer. The latent heat flux at the test surface is always zero, since the surface is dry. The heat capacity of styrene foam is so small that the thermal conduction $G$ into the surface is small. The test surface is painted black, having an albedo $ref = 0.074$. An experiment for

a weak sensible heat flux was also conducted, which was realized by covering the window with a semitransparent film to reduce the shortwave flux at the horizontal test surface.

The heat balance on the test surface is described by

$$H = Rn - G, \tag{7.9}$$

$$Rn = (1 - ref)S + \sigma({T_\mathrm{W}}^4 - T_\mathrm{S}^4), \tag{7.10}$$

$$G = c_\mathrm{s}\rho_\mathrm{s} \int_0^z \frac{\partial T_\mathrm{g}(z)}{\partial t}\, dz, \tag{7.11}$$

where $Rn$ is the net radiation, $S$ the solar radiation incident on the horizontal test surface, $c_\mathrm{s}\rho_\mathrm{s}(= 32.2 \times 10^3\,\mathrm{J\,K^{-1}\,m^{-3}})$ the heat capacity of the styrene foam, $T_\mathrm{S}$ the test surface temperature, $T_\mathrm{g}(z)$ the styrene foam temperature at depth $z$(m), and $z$ the height from the test surface. The height of experimental room is 2.65 m, the width 4 m, and the length 6.55 m.

Value of $T_\mathrm{g}(z)$ were measured at heights of $z = -0.01, -0.02, -0.07, -0.12$ m by thermocouples, the representative air temperature in the room $T$ is measured at $z = 1.5$ m by a ventilated thermometer, and $S$ determined at a location next to the test surface by a pyranometer. The values of $Rn$, $G$, and $H$ are averaged over every 30 minutes, observation with the value of $C_\mathrm{H}U$ ($U \to 0$) then obtained through the bulk formula given by equation (7.1).

### 7.3.2 Rough Surface

Experiments on the rough surface are carried out in a manner similar to those on the smooth surface. To create a black rough surface, small aluminum cubes painted black were arranged on the thin black painted aluminum surface above styrene foam used in 7.3.1. The length and width of each cube are 0.02 m. The cubes create region of sun and shadow. However, the surface temperature of the surface is almost uniform, since the heat conductivity of the cube is sufficiently large. The representative temperature of the surface is measured on the surface of the cube.

Figure 7.3 shows arrangements for various horizontal density of the roughness elements $r$ with constant height $h$. ($r$ is area ratio of roughness elements.) For the case of the sparsest conditions ($r = 1/32$), the cubes were settled on squares written "1/32". Then in order of increasing $r$, the number of the settled cubes are doubled. Figure 7.4 shows the illustration of built-up cubes with constant density $r$. The height is changed to $h = 4, 6$ cm.

## 7.4 Results

### 7.4.1 Smooth Surface

Figure 7.2 displays the relationship between $H$ and $T_S - T$ calculated from the experimental data. The error is estimated at $\pm 1$ °C for $T_S - T$ and $\pm 15\,\mathrm{W\,m^{-2}}$ for $H$. Therefore, the data in this figure are limited to value of $T_S - T > 5$ °C. The number of data meeting this criterion is 98.

The straight line in Figure 7.2 represents $C = 1.4$, therefore the coefficient $b$ in $C_H U = b\,(T_S - T)^{1/3}$ was determined by a least squares fit as

$$b = 0.0011 \qquad \mathrm{m\,s^{-1}\,K^{-1/3}}. \tag{7.12}$$

This values of $C$ and $b$ are confirmed that they are valid for field (Kondo and Ishida, 1997).

### 7.4.2 Rough Surface

The values of $C$ and $b$ for the rough surface are evaluated with the arrangements of the cubes illustrated in Figure 7.3 and 7.4. The corresponding results are shown in Figure 7.5 and 7.6, respectively. Of course, when the roughness elements are settled, the coefficient $C$ is larger than the smooth case. But $C$ is not increasing uniformly with $r$, $C$ has a maximum value (Figure 7.5). The possible reason is that too dense roughness arrangement does not remain sufficient space where plumes are produced.

Figure 7.6 shows the results when the height of roughness elements are changed. The higher roughness elements makes the larger value of $C$. However, the increment of $C$ when $h = 4 \rightarrow 6$ cm is smaller than when $h = 2 \rightarrow 4$. It indicates that the increment of $C$ is not uniform with $h$.

These results are gotten together and comparing with height-distance ratio $h/d$ in Figure 7.7, where $d$ is average distance between the arranged roughness elements. And corresponding values of $r$ are written in Table 7.2. Since the surface area including the roughness elements increases when the number of roughness elements increases, it should be considered that the sensible heat flux is larger because of this increasing surface area effect. The open circle points of Figure 7.7 shows the value of $C$ per unit surface area.

According to above results, $C$ has a maximum value when the height-distance ratio $h/d$ is appropriate, but this maximum value maybe change with the height of roughness elements $h$.

## 7.5 Concluding Remarks

Under natural convective conditions, it is found by the indoor experiments that the bulk exchange speed $C_{\mathrm{H}}U$ is only function of the temperature difference $T_{\mathrm{S}} - T$ (equation (7.7)). Therefore, the sensible heat flux can be expressed as $H = C(T_{\mathrm{S}} - T)^{4/3}$ under these conditions. And $C$ and $b$ in equation (7.7) has a maximum value when the height-distance ratio $h/d$ is appropriate. These results indicate the existence of optimum value of $h/d$ to create plumes. In other words, sufficient horizontal space is needed for creating strong plumes to transfer the sensible heat. According to Chapter 6, the vertical component of TKE produced by the buoyancy tends to be released into horizontal directions through the pressure correlation term under strongly unstable conditions. This result supports that there is an optimum vertical-horizontal ratio to develop convections, such as the Rayleigh–Bénard convection (Rayleigh, 1916).

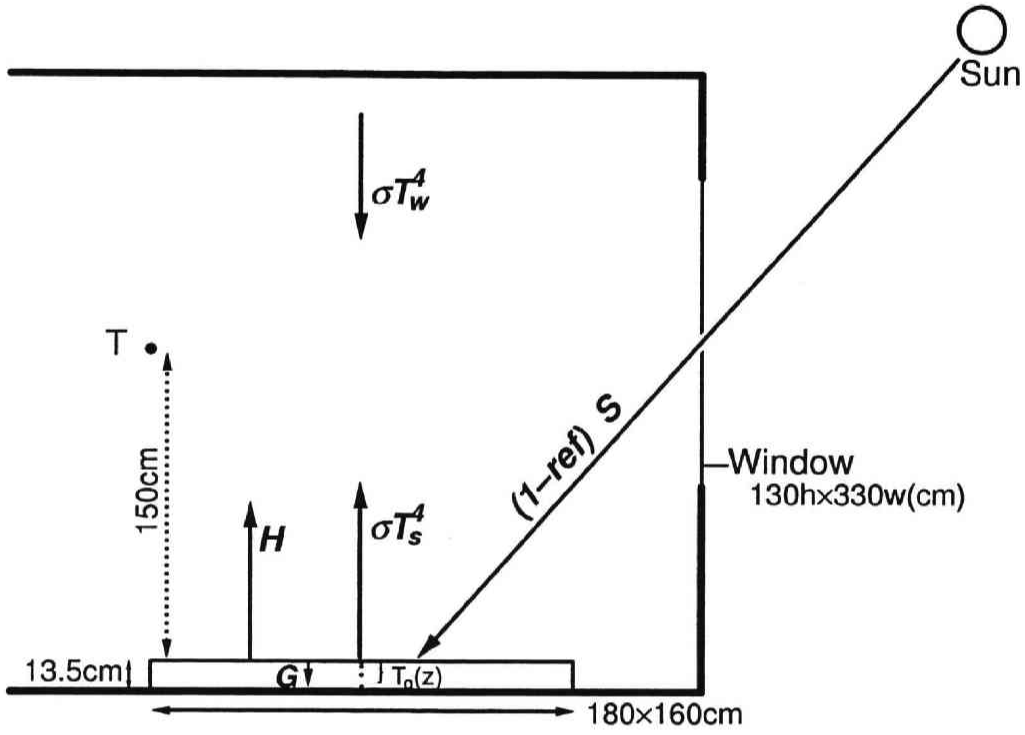


Figure 7.1: Conceptual illustration of the setup for the indoor experiments.

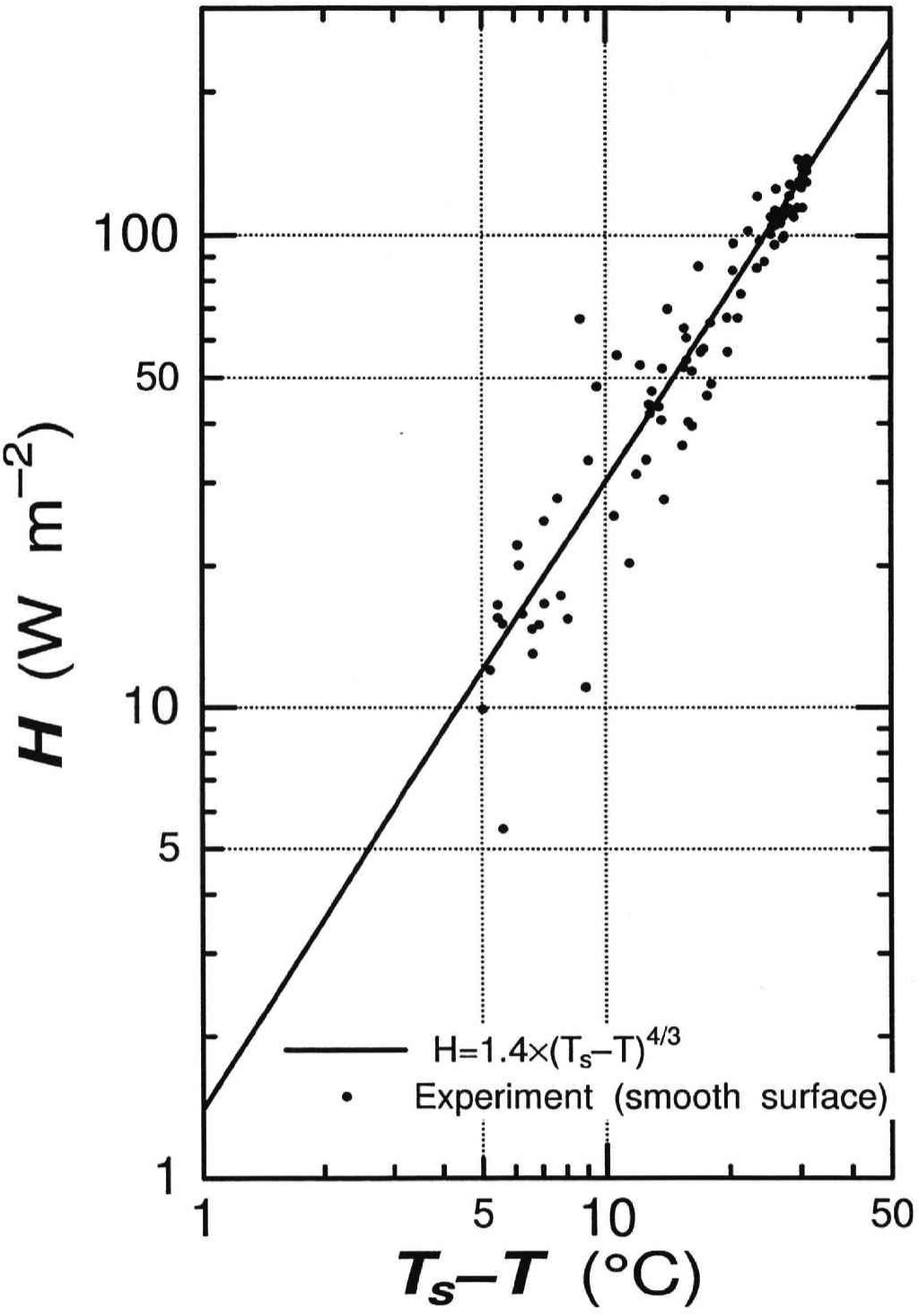


Figure 7.2: Relationship between $T_S - T$ and $H$ over the smooth surface of the indoor experiment. After, Kondo and Ishida (1997).

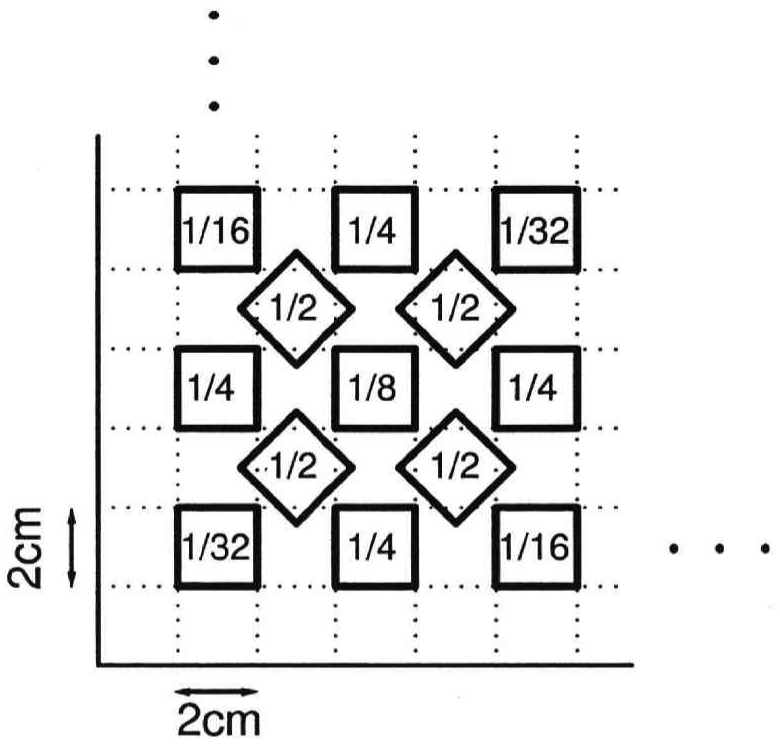


Figure 7.3: Downward view of horizontal arrangements of the roughness elements.

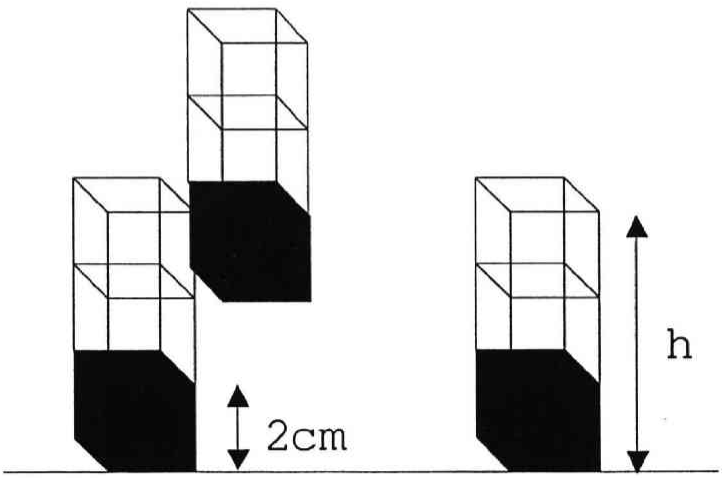


Figure 7.4: Conceptual illustration of built-up roughness elements.

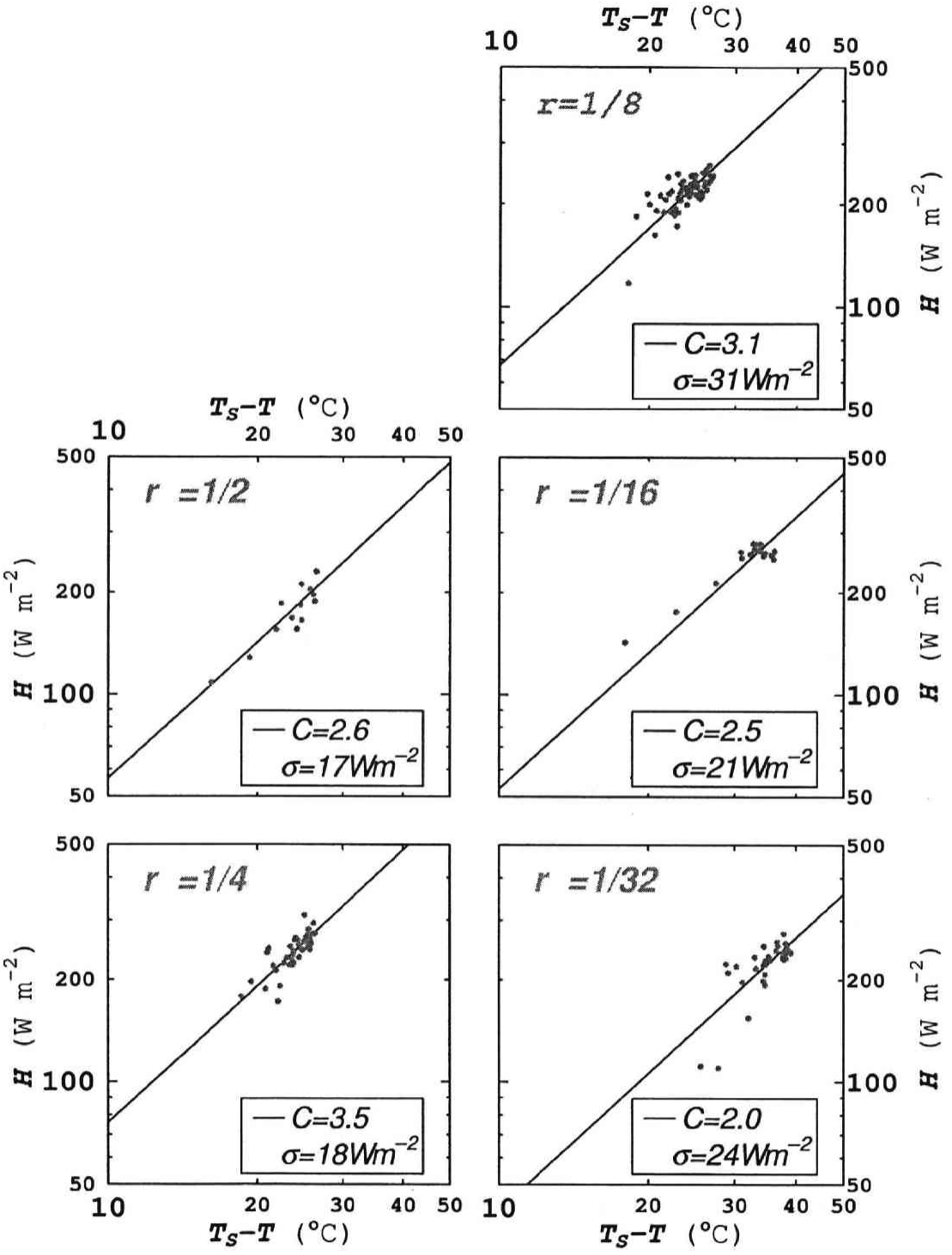


Figure 7.5: Relationships between the temperature difference $T_S - T$ and sensible heat flux $H$ with changes in roughness elements density.

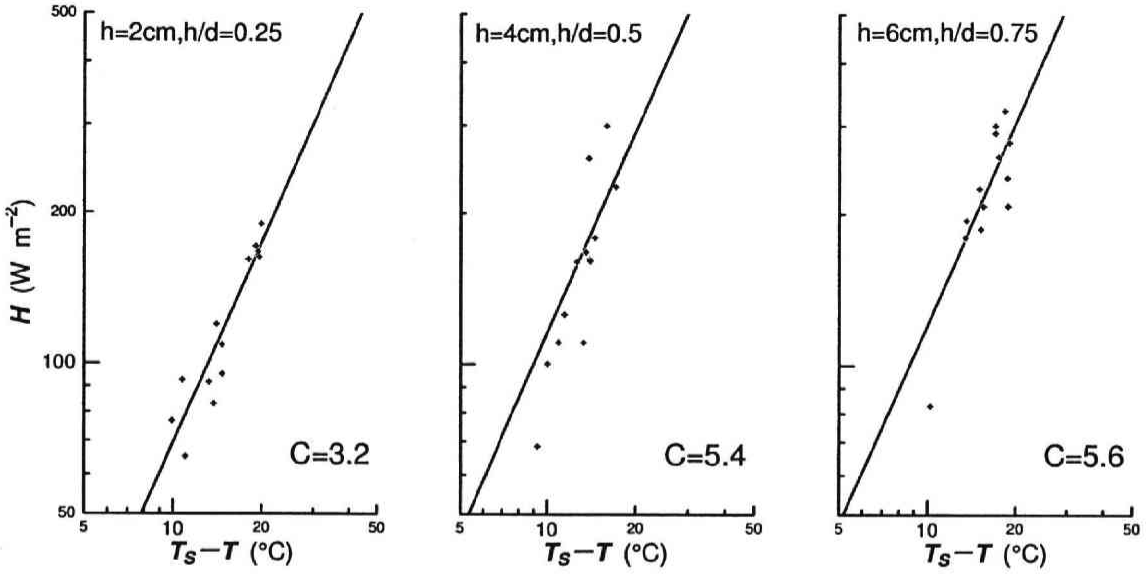


Figure 7.6: Relationships between the temperature difference $T_S - T$ and sensible heat flux $H$ with changes in roughness elements height.

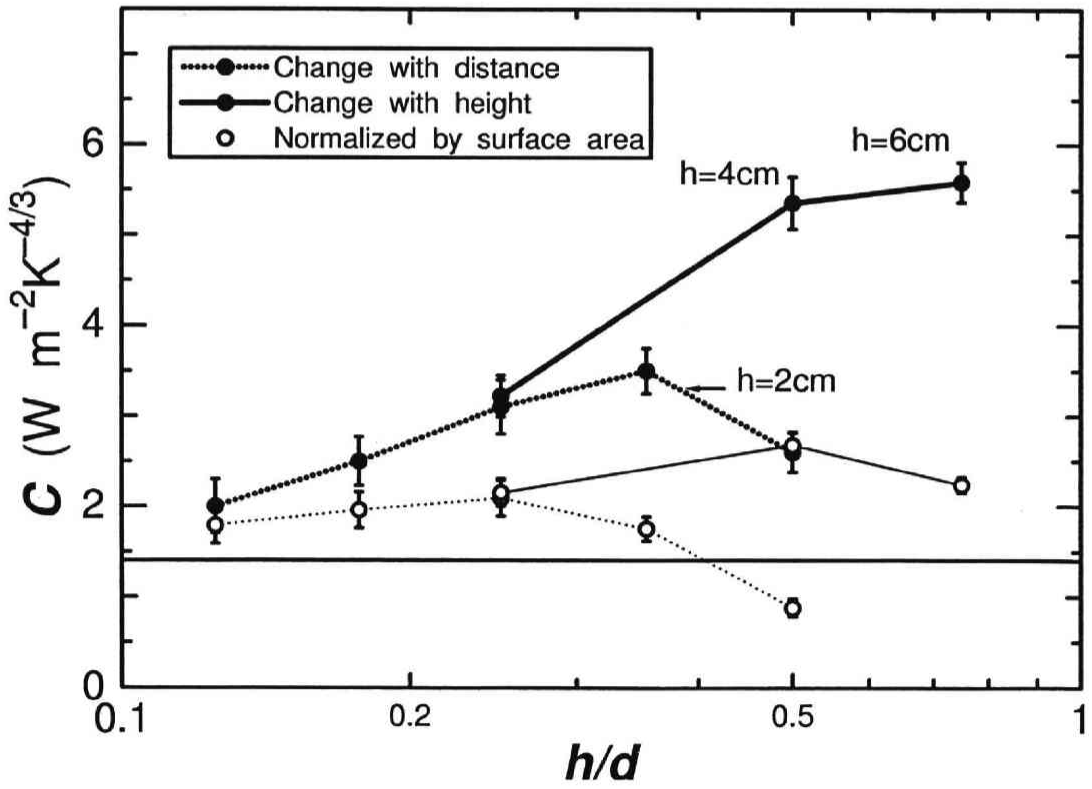


Figure 7.7: Relationship between the height-distance ratio $h/d$ and the heat transfer coefficient $C$.

Table 7.1: The coefficients $A$ and $a$ in $Nu = A \times Ra^a$, and $b$ in $C_H U = b(T_S - T)^{1/3}$ over the respective range of $Ra$ in several engineering heat transfer experiments.

| References | $Ra$ | $a$ | $b \times 10^3$ | $A$ | Samples |
|---|---|---|---|---|---|
| Lloyd and Moran (1974) | $2.2 \times 10^4 \sim 8 \times 10^6$ | 1/4 | — | 0.54 | $CuSO_4 + H_2SO_4$ |
| Fujii and Imura (1972)* | $10^5 \sim 2 \times 10^8$ | 1/3 | 1.6 | 0.16 | $H_2O$. |
| Lloyd and Moran (1974) | $8 \times 10^6 \sim 1.6 \times 10^9$ | 1/3 | 1.5 | 0.15 | $CuSO_4 + H_2SO_4$ |
| Mikheyev (1968) | $2 \times 10^7 \sim 10^{13}$ | 1/3 | 1.8 | 0.18 | Various fluids |
| Fujii and Imura (1972)* | $5 \times 10^8 \sim 10^{12}$ | 1/3 | 1.3 | 0.13 | $H_2O$. |
| Takeyama et al. (1983)** | $10^{10} \sim 10^{12}$ | 0.4 | — | 0.024 | Various fluids |

*: The surface is on the floor. **: $A$ for the horizontal case is estimated from the vertical value.

Table 7.2: The heat transfer coefficient $C$ in various arrangements of roughness elements.

| $h$ (cm) | $r$ | $h/d$ | $C$ ($Wm^{-2}K^{-4/3}$) |
|---|---|---|---|
| 2 | 1/32 | 1/8 | 2.0 |
| 2 | 1/16 | $1/4\sqrt{2}$ | 2.5 |
| 2 | 1/8 | 1/4 | 3.1 |
| 2 | 1/4 | $1/2\sqrt{2}$ | 3.5 |
| 2 | 1/2 | 1/2 | 2.6 |
| 4 | 1/8 | 1/2 | 5.4 |
| 6 | 1/8 | 3/4 | 5.6 |

# Chapter 8

# Conclusions

Each term and component of the Turbulent Kinetic Energy (TKE) equation is evaluated by using the field data in this study. Since the pressure correlation term is the most unknown part of this equation, the objective of this study focuses on understanding the role of the pressure correlation term.

As a first step, the TKE equation in each component is derived from the Navier–Stokes (NS) equation in Chapter 2. Due to the presence of the turbulent transport and pressure correlation terms that are derived from the nonlinear term of the NS equations, TKE equation cannot be solved analytically. Since the pressure correlation term was considered as a TKE redistribution term: neither production nor dissipation term, TKE of the $x_2$-component must be redistributed through the turbulent transport and/or pressure correlation terms. Therefore, these terms should be evaluated in order to understand the TKE properties of the $x_2$-component.

In Chapter 3, the horizontal homogeneity of the turbulent data for evaluation, which was obtained in the intensive observations using multiple turbulent sensors, was confirmed. These observations were performed on the uniform paddy field after harvest in 2002 and 2003. It is found that even on apparently homogeneous surface, the sensible heat flux is different among the sites. In CAPS2002, the difference of the sensible heat flux $H$ among the sites is correlated with the surface temperature and wind speed, and the each term of measured heat was not closed. This heat imbalance could cause heat advection. On the contrary, the heat balance was closed in CAPS2003. Therefore, the data of CAPS2003 is used for evaluation of each term of TKE.

In Chapter 4, in order to eliminate the temporal and spatial variations of the TKE and the horizontal strain (shear) of the wind environment, the coordinate system is transformed in 3 steps; further, the data for evaluating each term of the TKE are selected. After the data selection, 8.4% of the total data (369/4380) remains. The selected conditions related to horizontal homogeneity described in this study are original. This is probably why the results are different from those of conventional studies, particularly with regard to the horizontal components.

In Chapter 5, the relationships among the second-, third-, and fourth-order moments are shown. These results are related to the normality of the turbulence, and they can be used to solve the turbulent closure problems. The results of this chapter can be summarized as: 1) the normal distribution hypothesis can be applied to the higher-order moments of horizontal components ($u_1'$ and $u_2'$) but vertical one ($u_3'$); 2) most values of $\overline{u_1' u_3'}$ are distributed near the average.

In Chapter 6, each term and component of the TKE equation is quantified using the field data: this confirms the temporal and spatial homogeneity in Chapter 4. The results are summarized as follows:

- The shear production and dissipation term is consistent with the conventional results.
- The turbulent transport term of the horizontal components are almost zero, although the vertical component is significantly negative under unstable conditions.
- The total pressure correlation term gains the TKE under unstable conditions, and loses it under stable conditions. The results of each component indicate that this term redistributes the TKE isotropically from the longitudinal ($x_1$-) and vertical ($x_3$-) components to the lateral ($x_2$-) component. The source is the $x_1$-component under stable and weakly unstable conditions, and the $x_3$-component under strongly unstable conditions.

In Chapter 7, it is found by the indoor experiments that the bulk exchange speed for heat is only function of the temperature difference between the surface and air ($T_S - T$) under strongly unstable conditions. Therefore, the sensible heat flux can be expressed as $H = C(T_S - T)^{4/3}$ under these conditions. And $C$ has a maximum value over a rough surface, when the height-distance ratio $h/d$ of roughness elements is appropriate. These results indicate the existence of optimum value of $h/d$ to create plumes.

The results of TKE evaluation in this study are different from the conventional study. This difference could be determined by data screening. Data screening process probably eliminates the horizontally skewed data. On the basis of these results, the total pressure correlation term cannot be neglected. It is interesting that the pressure correlation term of the $x_3$-component is a source term of the TKE and redistribute to the horizontal components under strongly unstable conditions, even the horizontal components of TKE is larger than vertical one. Because of it, a sufficient horizontal space is needed for creating strong plumes to transfer the sensible heat in the indoor experiments under these conditions.

Numerical models are excellent solutions both for the meteorological and the environmental analysis. Recently, calculation at finer resolutions is required because of treating with heterogeneous surface such as urban buildings and forests. Since these surface conditions can easily strain the above turbulence environment, these terms derived from the nonlinear term can not be neglected and should be parameterized correctly by using the results of this study.

# Appendix

## A.1 List of Symbols

| | |
|---|---|
| $A$ | slope of the structure function or empirical constant of equation (7.6) |
| $a$ | absolute humidity* or empirical constant of equation (7.6) |
| $b$ | empirical constant of (7.7) |
| $C$ | empirical constant of equation (2.12) and (2.13) or (7.8) |
| $C_0$ | empirical constant of equation (6.14) |
| $C_H$ | bulk transfer coefficient for heat |
| $c_P$ | specific heat of air at constant pressure |
| $c_s\rho_s$ | heat capacity of styrene foam |
| $E$ | water vapor flux |
| $D$ | structure function |
| $d$ | average distance between the arranged roughness elements |
| $G$ | conductive soil heat flux |
| $Gr$ | Grashof number |
| $g$ | gravitational acceleration |
| $H$ | sensible heat flux |
| $h$ | height of roughness elements |
| Ku | kurtosis |
| $k$ | von Kármán constant |
| $L$ | Obukhov length |
| $Ln$ | net longwave radiation |
| $l$ | latent heat of evaporation or scale length of the natural convection |
| $l_1$ | empirical constant of equation (2.12) and (2.13) |
| $Nu$ | Nusselt number |
| $Pr$ | Prandtl number |
| $p$ | air pressure* |
| $q$ | total turbulent kinetic energy ($\equiv (\overline{u_i'^2})^{1/2}$)* |

| | |
|---|---|
| $R_{ij}, R_{i\theta}$ | second-order moment $(= \overline{u_i' u_j'}, \overline{u_i' \theta})^*$ |
| $R_{ijk}$ | third-order moment $(= \overline{u_i' u_j' u_k'})^*$ |
| $R_{ijkl}$ | fourth-order moment $(= \overline{u_i' u_j' u_k' u_l'})^*$ |
| $r$ | area ratio of roughness elements |
| $r_{ij}$ | normalized second-order moment $(= R_{ij}/u_*^2)^*$ |
| $r_{ijk}$ | normalized third-order moment $(= R_{ijk}/u_*^3)^*$ or skewness |
| $r_{ijkl}$ | normalized fourth-order moment $(= R_{ijkl}/u_*^4)^*$ or kurtosis |
| $Ra$ | Rayleigh number |
| $Rn$ | net radiation |
| $ref$ | albedo |
| $S$ | insolation |
| Sk | skewness |
| $Sn$ | net insolation |
| $T$ | air temperature* |
| $T_g$ | styrene foam temperature |
| $T_S$ | surface temperature |
| $T_W$ | effective infrared temperature of walls |
| $t$ | time |
| $U$ | scalar-averaged wind velocity |
| $u, v, w$ | $= u_1, u_2, u_3$ in Chapter 4 |
| $u_*$ | friction velocity |
| $u_i$ | a component of wind velocity* |
| $x_i$ | a component of distance* |
| $x, y, z$ | $= x_1, x_2, x_3$ in Chapter 4 |
| $z_0$ | roughness length for momentum |
| $z_T$ | roughness length for heat |
| | |
| $\beta$ | coefficient of thermal expansion |
| $\gamma$ | angle in Chapter 4 |
| $\delta_{ij}$ | Kronecker's delta* |
| $\varepsilon$ | dissipation rate |
| $\zeta$ | non-dimensional height $(= x_3/L$; stability) |
| $\eta$ | Kolmogorov's micro scale |
| $\Theta_v$ | virtual potential temperature if the environment |
| $\theta$ | potential temperature* or rotational angle in Chapter 4 |
| $\theta_v$ | virtual potential temperature* |

| | |
|---|---|
| $\kappa$ | thermometric conductivity |
| $\lambda_1$ | empirical length of equation (2.10) and (2.11) |
| $\nu$ | kinetic molecular viscosity |
| $\rho$ | air density |
| $\rho_0$ | reference air density |
| $\sigma$ | standard deviation or Stefan–Boltzmann constant |
| $\tau$ | time-lag |
| $\phi, \psi$ | rotational angle in Chapter 4 |
| $\phi_{\mathrm{H}}$ | non-dimensional function of temperature gradient |
| $\phi_{\mathrm{M}}$ | non-dimensional function of wind shear |
| $\phi_\varepsilon$ | non-dimensional dissipation rate |
| $\Psi$ | integral form of the $\phi$-function |

*subscript

| | |
|---|---|
| 1 | a component for longitudinal (the prevailing wind) direction |
| 2 | a component for lateral (orthogonal to $x_1$) direction |
| 3 | a component for vertical direction |
| $i,j,k,l$ | Einstein's summation notation |

*superscript

| | |
|---|---|
| $'$ | turbulent part |

| | |
|---|---|
| *overline | mean part or time averaged value |

## A.2 Sensors Lists Used in CAPS

Table A.1: Sensors used in CAPS2002. Sensors are listed in each north-south path. Only C4 site has three heights. SAT means sonic anemometer-thermometer, and IRGA is infrared gas analyzer. Observational area was so wide that the data loggers were installed at each site. Time differences of the data loggers are also described. The distribution of sites are shown in Figure 3.1.

| | Site | Height | SAT | IRGA | Time difference (trend, max.) | Remark |
|---|---|---|---|---|---|---|
| West | S10 | | DA-600-3T TR-61A (KAIJO) | | | "S0" in map |
| | S1 | 2.51m | DA-600-3T TR-61A (KAIJO) | | < +1s/day, +1s | |
| | S3 | 2.74m | SAT-550 (KAIJO) | | -2s/day, -17s | |
| | S5 | 2.46m | SAT-550 (KAIJO) | | -18.4s/day, -115s | |
| | S7 | 2.45m | DA-600-3T TR-61A (KAIJO) | | -15.3s/day, -78s | |
| Center | C1 | 2.45m | 1210R3 (Gill) | LI-7500 (Licor) | -5.25s/day, -41s | w: N/A |
| | C2 | 2.50m | DA-600-3T TR-61C (KAIJO) | AH-300 (KAIJO) | ±2s/day, -10s | |
| | C3 | 2.46m | USA-1 (Metek) | | <-1s/day, -3s | No IRGA |
| | C4(1) | 1.00m | DA-600-3T TR-62TZ (KAIJO) | | -4.5s/day, -27s | 3 heights |
| | C4(2) | 2.45m | DA-600-3T TR-61A (KAIJO) | LI-7500 (Licor) | | |
| | C4(3) | 5.90m | DA-600-3T TR-62A (KAIJO) | | | |
| | C5 | 2.35m | 1210R3 (Gill) | LI-7500 (Licor) | <-1s/day, -36s | w: N/A |
| | S9 | 2.47m | DA-600-1T TR-41 (KAIJO) | | -2.5s/day, -10s | 1 dimensional |
| East | S2 | 2.54m | 81000 (Young) | | +0.7s/day, +6s | sideways |
| | S4 | 2.38m | PAT-600 (KAIJO) | | +1.5s/day, +8s | |
| | S6 | 2.53m | DA-600-3T TR-61A (KAIJO) | | <±1s/day, <±1s | v: N/A (w,T only) |
| | S8 | 2.47m | DA-600-3T TR-61A (KAIJO) | | +6.5s/day, -51s | u: N/A |

Table A.2: Sensors used in CAPS2003. C3, N3 and S3 sites have three heights. The distribution of sites are shown in Figure 3.1.

| | Site | Height | SAT | IRGA | Remarks |
|---|---|---|---|---|---|
| N I S | N3(1) | 1.28m | Kaijo DA-600(TR-62AX) | | 3 heights |
| | N3(2) | 2.51m | Kaijo SAT-550 | | |
| | N3(3) | 5.00m | Kaijo DA-600(TR-61A) | | |
| | N2 | 2.50m | Campbell CSAT3 | | |
| | N1 | 2.55m | Kaijo DA-600(TR-62AX) | Li-Cor LI-7500 | 64ch logger* |
| | C(1) | 1.25m | Kaijo DA-600(TR-62AX) | | Center of the array 3 heights, 64ch logger |
| | C(2) | 2.56m | Kaijo DA-600(TR-61A) | Li-Cor LI-7500 | |
| | C(3) | 5.06m | Kaijo DA-600(TR-61B) | | |
| | S1 | 2.51m | Gill 1210R3 | Li-Cor LI-7500 | 64ch logger* |
| | S2 | 2.34m | Kaijo PA-600 | | |
| | S3(1) | 1.27m | Kaijo DA-600(TR-62AX) | | 3 heights |
| | S3(2) | 2.56m | Gill 1210R3 | | |
| | S3(3) | 5.00m | Gill 1210R3 | | |
| W I E | W1 | 2.50m | Kaijo SAT-550 | Advanet E009B | 64ch logger* |
| | E1 | 2.47m | Kaijo DA-600(TR-61A) | Li-Cor LI-7500 | 64ch logger* |
| | E2 | 2.54m | Kaijo SAT-550 | | |
| | E3 | 2.46m | Kaijo DA-600(TR-41) | | |

*: same logger

# References


Alberghi, S., A. Maurizi and F. Tampieri, 2002: Relationship between the vertical velocity skewness and kurtosis observed during sea-breeze convection. *J. Atmos. Sci.*, **41**, 885–889.

Anfossi, D., G. Degrazia, E. Ferrero, S. E. Gryning, M. G. Morselli and S. T. Castelli, 2000: Estimation of the lagrangian structure function constant $c_0$ from surface-layer wind data. *Bound.-Layer Meteor.*, **95**, 249–270.

Brutsaert, W., 1992: Stability correction functions for the mean wind speed and temperature in unstable surface layer. *Geophys. Res. Lett.*, **19**, 469–472.

Cuxart, J., G. Morales, E. Terradellas and C. Yagüe, 2002: Study of coherent structures and estimation of the pressure transport terms for the nocturnal stable boundary layer. *Bound.-Layer Meteor.*, **105**, 305–328.

Dwyer, M. J., E. G. Patton and R. H. Shaw, 1997: Turbulent kinetic energy budgets from a large-eddy simulation of airflow above and within a forest canopy. *Bound.-Layer Meteor.*, **84**, 23–43.

Dyer, A. J., and B. B. Hicks, 1970: Flux-gradient relationships in the constant flux layer. *Quart. J. Roy. Meteor. Soc.*, **96**, 715–721.

Fujii, T., and H. Imura, 1972: Natural convection heat transfer from a plate with arbitrary inclination. *Int. J. Heat Mass Transfer*, **15**, 755–766.

Garratt, J. R., 1992: *The atmospheric boundary layer.* Cambridge University Press, 316pp.

Godfrey, J. S., and E. J. Lindstorm, 1989: The heat budget of the western equatorial Pacific surface mixed layer. *J. Geophys. Res.*, **94**, 8007–8017.

Gryanik, V. M., and J. Hartmann, 2002: A turbulence closure for the convective boundary layer based on a two-scale mass-flux approach. *J. Atmos. Sci.*, **59**, 2729–2744.

Ishida, S., 1995: Observational and experimental studies on the sensible heat flux under natural convective conditions. *Master's thesis*, 54pp. (in Japanese).

Ishida, S., D. Matsushima, A. Higuchi, T. Hiyama, M. Toda, J. Asanuma, I. Tamagawa, S. Miyazaki, K. Tanaka, M. Sugita, H. Nagai, H. Tanaka, S. Iida and N. Kobayashi, 2004a: Intensive field campaign 2001: Preliminary results in inter-comparison of the turbulent sensors. *J. Japan Soc. Hydrol. & Water Resour.*, **17**, 43–60 (in Japanese).

Ishida, S., K. Tanaka, A. Higuchi, I. Tamagawa, D. Matsushima and CAPS2002-2003 observation group, 2004b: Surface heat balance using flux measurement array during Catch A Plume by SATs (CAPS) IOP. *Proceedings of CD-ROM of The 6th International Study Conference on GEWEX in Asia and GAME, GAME CD-ROM Publication*, **11**, T1SI09Aug04111047.

Kaimal, J. C., J. E. Gaynor and H. A. Zimmerman, 1990: Minimizing flow distortion errors in a sonic anemometer. *Bound.-Layer Meteor.*, **53**, 103–115.

Kanda, M., R. Moriwaki, M. Roth and T. R. Oke, 2002: Area-averaged sensible heat flux and a new method to determine zero-plane displacement length over an urban surface using scintillometry. *Bound.-Layer Meteor.*, **105**, 177–193.

Kondo, J., and S. Ishida, 1997: Sensible heat flux from the earth's surface under natural convective conditions. *J. Atmos. Sci.*, **54**, 498–509.

Kondo, J., O. Kanechika and N. Yasuda, 1978: Heat and momentum transfers under strong stability in the atmospheric surface layer. *J. Atmos. Sci.*, **6**, 1012–1021.

Kormann, R., and F. X. Meixner, 2001: An analytical footprint model for non-neutral stratification. *Bound.-Layer Meteor.*, **99**, 207–224.

Lloyd, J. R., and W. R. Moran, 1974: Natural convection adjacent to horizontal surface of various planforms. *J. Heat Transfer*, **96**, 443–447.

Matsushima, D., T. Tanaka, S. Ishida, I. Tamagawa, A. Higuchi and CAPS2002 observation members, 2004: Surface temperature measurements by airplane and footprint analysis of the sensible heat flux. *Proceedings of 2004 annual conference, Japan Society of Hydrology and Water Resources*, 228–229 (in Japanese).

McMillen, R. T., 1988: An eddy correlation technique with extended applicability to nonsimple terrain. *Bound.-Layer Meteor.*, **43**, 231–245.

Mellor, G. L., 1973: Analytic prediction of the properties of stratified planetary surface layers. *J. Atmos. Sci.*, **30**, 1061–1069.

Mellor, G. L., and T. Yamada, 1974: A hierarchy of turbulence closure models for planetary boundary layers. *J. Atmos. Sci.*, **31**, 1791–1806.

Mikheyev, M., 1968: *Fundamentals of Heat Transfer.* Peace Publishers, 376pp.

Miles, N. L., J. C. Wyngaard and M. J. Otte, 2004: Turbulent pressure statistics in the atmospheric boundary layer from large-eddy simulation. *Bound.-Layer Meteor.*, **113**, 161–185.

Monin, A. S., and A. M. Yaglom, Eds., 1971: *Statistical Fluid Mechanics.* MIT Press, 769pp.

Rayleigh, L., 1916: On convection currents in a horizontal layer of fluid, when the higher temperature is on the under side. *Philos. Mag.*, **32**, 529–546.

Rotta, J. C., 1951: Statistische theorie nichthomogener turbulenz. *Z. Phys.*, **129**, 547–572.

Seager, R., S. E. Zebiak and M. A. Cane, 1988: A model of the tropical Pasific sea surface temperature climatology. *J. Geophys. Res.*, **93**, 1265–1280.

Skyllingstad, E. D., 2003: Large-eddy simulation of katabatic flows. *Bound.-Layer Meteor.*, **106**, 217–243.

Sugawara, H., 2001: Heat exchange between urban structures and the atmospheric boundary layer. *Doctral dissertation*, 140pp.

Takeyama, T., S. Ooya and T. Aihara, 1983: *Heat Transfer.* Maruzen, 254pp. (in Japanese).

Tamagawa, I., K. Tanaka, S. Ishida, A. Higuchi, D. Matsushima, J. Asanuma, K. Ono, T. Tada, T. Hayashi, H. Ishikawa, H. Tanaka, T. Hiyama, T. Iwata, K. Tanaka, E. Nakakta and CAPS Observation Group, 2004: Overview of intensive field campaign for Lake-Biwa Project 2002, Catch a Plume by SATs : CAPS. *J. Japan Soc. Hydrol. & Water Resour.*, **17**, 392–400 (in Japanese).

Thiermann, V., and H. Grassl, 1992: The measurement of turbulent surface-layer fluxes by use of bichromatic scintillation. *Bound.-Layer Meteor.*, **58**, 367–389.

Weare, B. C., 1989: Uncertainties in estimates of surface heat fluxes derived from marine r eports over the tropical and subtropical oceans. *Tellus*, **41A**, 357–370.

Wieser, A., F. Fiedler and U. Corsmeier, 2001: The influence of the sensor design on wind measurements with sonic anemometer systems. *J. Atmos. Oceanic Technol.*, **106**, 85–100.

Wyngaard, J. C., and O. R. Côté, 1971: The budgets of turbulent kinetic energy and temperature variances in the atmospheric surface layer. *J. Atmos. Sci.*, **28**, 190–201.

Wyngaard, J. C., O. R. Côté and Y. Izumi, 1971: Local free convection, similarity, and the budgets of shear stress and heat flux. *J. Atmos. Sci.*, **28**, 1171–1182.

Wyngaard, J. C., A. Siegel and J. M. Wilczak, 1994: On the response of a turbulent-pressure probe and the measurement of pressure transport. *Bound.-Layer Meteor.*, **69**, 379–398.